Improving Cardiovascular Stent Design Using Patient-Specific Models and Shape Optimization

Timothy J. Gundert
Marquette University

IMPROVING CARDIOVASCULAR STENT DESIGN USING PATIENT-SPECIFIC MODELS AND SHAPE OPTIMIZATION

by

Timothy J. Gundert

A Thesis submitted to the Faculty of the Graduate School,
Marquette University,
in Partial Fulfillment of the Requirements for
the Degree of Master of Science

Milwaukee, Wisconsin

December 2011

ABSTRACT
IMPROVING CARDIOVASCULAR STENT DESIGN USING PATIENT-SPECIFIC MODELS AND SHAPE OPTIMIZATION

Timothy J. Gundert

Marquette University, 2011

Stent geometry influences local hemodynamic alterations (i.e. the forces moving blood through the cardiovascular system) associated with adverse clinical outcomes. Computational fluid dynamics (CFD) is frequently used to quantify stent-induced hemodynamic disturbances, but previous CFD studies have relied on simplified device or vascular representations. Additionally, efforts to minimize stent-induced hemodynamic disturbances using CFD models often only compare a small number of possible stent geometries. This thesis describes methods for modeling commercial stents in patient-specific vessels along with computational techniques for determining optimal stent geometries that address the limitations of previous studies.

An efficient and robust method was developed for virtually implanting stent models into patient-specific vascular geometries derived from medical imaging data. Models of commercial stent designs were parameterized to allow easy control over design features. Stent models were then virtually implanted into vessel geometries using a series of Boolean operations. This approach allowed stented vessel models to be automatically regenerated for rapid analysis of the contribution of design features to resulting hemodynamic alterations. The applicability of the method was demonstrated with patient-specific models of a stented coronary artery bifurcation and basilar trunk aneurysm to reveal how it can be used to investigate differences in hemodynamic performance in complex vascular beds for a variety of clinical scenarios.

To identify hemodynamically optimal stents designs, a computational framework was constructed to couple CFD with a derivative-free optimization algorithm. The optimization algorithm was fully-automated such that solid model construction, mesh generation, CFD simulation and time-averaged wall shear stress (TAWSS) quantification did not require user intervention. The method was applied to determine the optimal number of circumferentially repeating stent cells (N_C) for a slotted-tube stents and various commercial stents. Optimal stent designs were defined as those minimizing the area of low TAWSS. It was determined the optimal value of N_C is dependent on the intrastrut angle with respect to the primary flow direction. Additionally, the geometries of current commercial stents were found to generally incorporate a greater N_C than is hemodynamically optimal.

The application of the virtual stent implantation and optimization methods may lead to stents with superior hemodynamic performance and the potential for improved clinical outcomes. Future *in vivo* studies are needed to validate the findings of the computational results obtained from the methods developed in this thesis.

ACKNOWLEDGEMENTS

Timothy J. Gundert

First, I want express my sincere gratitude to my advisor and mentor, Dr. LaDisa. He kindly allowed me to join his lab as an undergraduate and has since provided me with a wealth of opportunities to explore numerous research interests. In addition to his technical assistance, I am very grateful for the guidance he gave me in the many discussions we had about my career goals. I know I will continue to seek his advice long after I leave Marquette.

I sincerely appreciate the time and effort of all the members of my committee, Dr. Marsden, Dr. Ellwein and Dr. Foley, in preparing this thesis. I especially enjoyed collaborating with Dr. Marsden and her lab at UCSD. The optimization work presented in this thesis was largely the result of the advancements made in her research. Also, I want to thank Dr. Ellwein for her friendship and numerous engaging discussions that improved the quality of this work.

I would like to acknowledge several other collaborators with whom I have had the privilege to work with during my graduate career. I want to thank Dr. Shadden for sharing his technical expertise and the computer code which greatly enhanced the CFD quantification techniques described in this thesis. Though I did not work with them on the work presented here, I would like to recognize Dr. Migrino and Leanne Harmann at the Medical College of Wisconsin. They were both very patient and taught me several important lessons while working with them on my first research project as an undergraduate student.

I want to acknowledge Dr. Olson, Dr. Audi and Dr. Ropella within Marquette's Department of Biomedical Engineering. Dr. Olson was instrumental in helping me obtain a teaching assistant position within the department and ease the financial burden of graduate school. As a teaching assistant, it was pleasure to work with Dr. Audi. I also want to thank Dr. Audi for his encouragement and advice when I was deciding to go to graduate school. I want to acknowledge Dr. Ropella for her support of my research and helping me obtain travel funding to several conferences. The opportunity to interact with leaders in the field has undoubtedly improved the quality of my research.

Though I have already mentioned Dr. Olson, I would like to recognize his and Dr. Struble's efforts in obtaining a new computer cluster at Marquette (CBET-0521602). It would not have been possible to investigate optimal stent designs without the increased computational power provided by the new cluster. I also learned a lot from the high performance computing boot camp and seminars organized by Drs. Olson and Struble. Similarly, I wish to thank David Herzfeld for sharing his knowledge of high performance computing with me. He was a great resource when I was developing code to fully-automate CFD on the new cluster.

I want to thank my friends and colleagues in the Laboratory for Translational, Experimental and Computational Cardiovascular Research, Dave Wendell, Arjun Menon, Andrew Williams, Ronak Dholakia, Sara Nomeland, Sung Kwon, Hongfeng Wang and DJ Quam. Over the past few years I have enjoyed many intriguing discussions and probably just as many laughs with you.

Additionally, I want to acknowledge the funding source for my second year of graduate research, the Translational Opportunity Grant of the Pilot and Collaborative Clinical and Translational Research Grants program from the Clinical and Translational Science Institute of Southeastern Wisconsin. By alleviating me of my teaching assistant responsibilities, this grant provided me with additional time to focus on my research.

Finally, I owe my deepest gratitude to my parents, Jack and Karen. None of my success would be possible without their loving support and guidance. I also want to thank my siblings, Mike and Tracy, for being incredible role models throughout my life and I very grateful for the encouragement of you and your families during my time in graduate school.

TABLE OF CONTENTS

LIST OF TABLES

LIST OF FIGURES

LIST OF ACRONYMS

BMS = bare-metal stent

BP = blood pressure

CAD = computer aided design

CDF = cumulative distribution function

CFD = computational fluid dynamics

DES = drug-eluting stent

FEA = finite element analysis

KE = kinetic energy

LAD = left anterior descending coronary artery

LHS = latin hypercube sampling

LV = large vessel

MADS = mesh adaptive direct search

MET = mean exposure time

OSI = oscillatory shear index

PDF = probability density function

SMC = smooth muscle cell

SMF = surrogate management framework

SV = small vessel

TAC = total arterial compliance

TAWSS = time-averaged wall shear stress

TKE = turbulent kinetic energy

VTK = Visualization Toolkit

WSS = wall shear stress

Chapter 1

Background and Specific Aims

1.1 Stents for the treatment of cardiovascular disease

Cardiovascular stents are commonly used as vessel scaffolding to alleviate an arterial narrowing or stenosis and restore blood flow to the distal vasculature. Since their inception in the mid 1980s, stents have gained popularity in the medical community because they allow diseased vessels to be treated using minimally invasive surgical techniques thereby reducing the trauma, cost and many complications associated with traditional surgery. Though stents have primarily been used to treat stenosis within coronary arteries, they have also been adopted for treating peripheral arteries, such as the carotid, renal and femoral arteries [20, 99].

In addition to being used as vessel scaffolding, stents have recently been used as flow diversion devices. When used as flow diverting devices, stents are placed across aneurysms with the goal of occluding blood flow to the aneurysm and preventing potential rupture. Not to be confused with stent-grafts (fabric covered stents), flow diverting stents are not covered and rely on low porosity designs to alter blood flow. To date these devices have most commonly been used to treat intracranial aneurysms [22].

Despite widespread use and several decades of research, the success of cardiovascular stents has been limited in some cases by adverse clinical outcomes. In-stent restenosis, or a re-narrowing of a previously treated vessel due to excessive tissue growth, is the primary complication following stent implantations across all vascular beds. In the coronary vasculature, restenosis requiring revascularization occurs in over 20% of patients [23, 76]. Rates of restenosis between 10-15% have also been reported in the peripheral arteries [4, 106, 110]. In an effort to reduce restenosis, drug-eluting stents (DES) have been developed in which bare-metal stents (BMS) are coated with an antiproliferative pharmaceutical agent to suppress smooth muscle cell (SMC) growth that leads to restenosis. Though DES have decreased the incidence of restenosis compared to BMS, retrospective studies of DES still report restenosis rates as high as 10% [48, 67, 74, 121]. Moreover, by inhibiting SMC growth, DES also inhibit the growth or migration of endothelial cells atop stent struts [32, 46]. The lack of a confluent layer of endothelial cells over stent struts increases the susceptibility of the artery to late stent thrombosis. In the coronary vasculature, the incidence of late stent thrombosis is only 1%, but it results in acute myocardial infarction in 40-70% of cases [44, 55]. DES are less commonly used in the peripheral arteries, but it should be noted that late stent thrombosis in supra-aortic arteries can result in ischemic stroke [20].

As noted above, advancements in stent technology have decreased the prevalence of adverse clinical outcomes to about 10%, but the affected population is still rather large given that over one million stents are implanted each year [28]. Based on a large body of evidence suggesting hemodynamic forces influence the vascular response following stent

implantation, this thesis aims to develop new techniques to investigate these forces with the goal of further improving stent design and clinical outcomes.

1.2 Patterns of wall shear stress influence the progression of cardiovascular disease

Wall shear stress (WSS), defined as the tangential force imposed on the vessel wall by blood flow, plays an important role in the autoregulation of vessel caliber and vascular remodeling. In general, arteries remodel to preserve a homeostatic level of WSS. Increases in WSS caused by a decreased lumen diameter or increased flow have been shown to cause outward arterial remodeling [36, 47]. Furthermore, extremely high values of WSS are associated with vessel remodeling responsible for aneurysm initiation and progression [38, 102]. Conversely, regions of low WSS correlate with inward vascular remodeling and the progression of atherosclerosis [54]. This relationship between vascular remodeling and WSS suggests that stents designed to preserve the homeostatic level of WSS may suppress the progression of atherosclerosis and tissue growth that leads to restenosis.

1.3 Stent implantation alters local hemodynamics

Though stents are designed to reduce alterations in hemodynamics that lead to atherosclerosis and aneurysm formation, stent implantation may also induce detrimental changes in the local hemodynamic environment. Stents impart a chronic radial force resulting in a large compliance mismatch between the vessel and the more rigid stent [15, 57]. The disparity in compliance at the ends of the stent introduces sites of pressure wave reflection that create flow disturbances in the stented vessel [1, 80]. More importantly, stent implantation introduces localized areas of low WSS and flow stagnation near stent

struts [16, 56]. In an *in vivo* study of stents implanted in rabbit iliac arteries, it was determined that these areas strongly correlate with increased neointimal hyperplasia that leads to restenosis [63]. Additionally, areas of complex flow near stent struts facilitate platelet deposition onto the arterial wall which likely affects the progression of late stent thrombus formation in the absence of a confluent layer of endothelial cells [24, 29].

1.4 Design and geometry affect the outcome of stent implantation

Not all stents alter local hemodynamics in the same manner. Previous animal studies indicate that the arterial response to stent implantation varies depending on the stent design. For example, Rogers and Edelmen studied the difference between coronary stent designs by implanting stents with two different configurations but identical diameters, surface area and material into the iliac arteries of rabbits [93]. They found that simply changing the stent configuration could reduce vascular injury, thrombus and neointimal hyperplasia. Similarly, Sadasivin *et al*. induced saccular aneurysms in rabbit carotid arteries to analyze various flow diverting stents and determined that increased pore density generated a greater amount of flow stasis in the aneurysm subsequently improving stenting success [94]. In both of these examples, the disparity in stent performance can likely be attributed to the difference in the hemodynamic environment create by the stent geometry.

1.5 Quantifying stent-induced changes in hemodynamics

Hemodynamic indices (i.e. pressure, velocity, WSS etc.) associated with stent implantation are difficult to quantify *in vivo*. Noninvasive imaging techniques such as ultrasound and phase-contrast magnetic resonance imaging can measure *in vivo* blood

velocity, but these systems lack the resolution necessary to accurately compute WSS following stenting implantation [50]. Even if imaging systems could accurately measure WSS, often these systems only quantify WSS in a two-dimensional plane. Computational fluid dynamics (CFD) provides a practical means of modeling arterial blood flow to overcome the limitations of current imaging technology. Assuming the vessel geometry and blood flow can be accurately recreated, CFD models enable hemodynamic indices to be quantified in three dimensions, and the use of high density computational meshes facilitates the detailed investigation of hemodynamic indices near stent struts. Furthermore, CFD can be used to provide estimates of stent performance without necessitating the high cost of stent manufacturing or clinical models.

1.6 Thesis motivation and specific aims

While previous CFD studies of stent performance have been invaluable, they have often been confined to simplified stent models, idealized vascular representations and only compare a handful of possible designs. The objective of this thesis is to address these limitations by developing robust computational methods to better evaluate current and emerging stent designs based on their hemodynamic performance. The development of these tools can be organized into the two specific aims described below.

SPECIFIC AIM 1: Develop and demonstrate a rapid and computationally inexpensive method to virtually implant current and next-generation stents into patient-specific computational fluid dynamics models

This investigation builds on a previously described methodology for modeling stents in simple patient-specific geometries reconstructed from medical imaging data [116]. The method is improved to facilitate the modeling stents in complex patient geometries and rapid parametric analysis of commercially available stent designs. Additionally, advanced quantification methods are developed to analyze hemodynamic stent performance within irregular patient-specific geometries. The applicability of the method is demonstrated using patient-specific models of a stented coronary artery bifurcation and basilar trunk aneurysm.

SPECIFIC AIM 2: Construct a computational framework which couples an established optimization algorithm with computational fluid dynamics to improve cardiovascular stent design.

The solid model generation, CFD simulation and WSS quantification used to evaluate stent performance is coupled with the surrogate management framework [73] to construct a fully-automated computational algorithm for optimizing stent designs. The framework is used to determine the optimal configurations of a simple slotted-tube stent along with three commercially available coronary stent designs.

Chapter 2

A Rapid and Computationally Inexpensive Method to Virtually Implant Current and Next-Generation Stents into Patient-Specific Computational Fluid Dynamics Models

2.1 Introduction

Computational fluid dynamics is often used to quantify hemodynamic alterations induced by stenting, but frequently uses simplified computational models of deployed stents and idealized vascular geometries [60, 61]. Solid mechanics, or finite element analysis (FEA), studies of stent expansion with subsequent flow analysis undoubtedly offer an ideal approach for scrutinizing devices, but involve several potential limitations. For example, these studies are typically performed with only a portion of the stent, representing a few millimeters in length, but the typical length of stents implanted in the superficial femoral arteries can exceed 100 mm in length. A finite element approach may also require the non-trivial process of converting a discrete finite element mesh into a parametric surface to create CFD meshes [11]. Moreover, patient-specific modeling of stent implantation using solid mechanics would further increase the time and computational cost of an already computationally expensive CFD simulation process. As a result, a full-scale analysis of this type is rare.

The objective of this investigation was to develop a rapid and robust method for assessing the influence of current and next-generation stents on patient-specific local

hemodynamics and vascular biomechanics quantified by CFD. As opposed to a full-scale approach of solid mechanics modeling with subsequent CFD, the post-implantation deformation of strut linkages for a portion of the investigated stent is determined using finite element analysis or microscopy if the expanded orientation of linkages is not previously known, and computer aided design (CAD) is then used to propagate the knowledge of strut deformation throughout the full length of a stent for virtual implantation into patient-specific CFD models. The sections below begin with a description of the methods used to virtually implant commercially available, next generation or prototype stents within a CFD model along with techniques for quantifying their hemodynamic performance. The use of this new method is then applied in two case studies using patient-specific CFD models generated from the coronary and cerebral portions of the arterial vasculature. Importantly, each of these examples highlights the use of these methods to investigate current clinical sequelae and potential sources of long-term morbidity thought to be influenced by adverse hemodynamic alterations.

2.2 Model construction and simulation methods

2.2.1 Patient-specific CFD model creation

Computational representations of the vasculature were created using Simvascular open-source software (https://simtk.org/home/simvascular), which facilitates volume visualization and conversion of medical imaging data into geometrically representative computer models (Figure 2.1: A1-A3). The process involves finding the centerline path of each artery, performing segmentation to delineate the arterial wall and connecting these segments to form a Parasolid model (Siemens, Plano, TX)[118]. In cases where the stent-to-artery deployment ratio used clinically would alter the global geometry within

the stented region (i.e. for balloon-expandable stents) physician guidance is required to alter segments within the stented region of the vessel according to standard interventional procedures [93, 109].

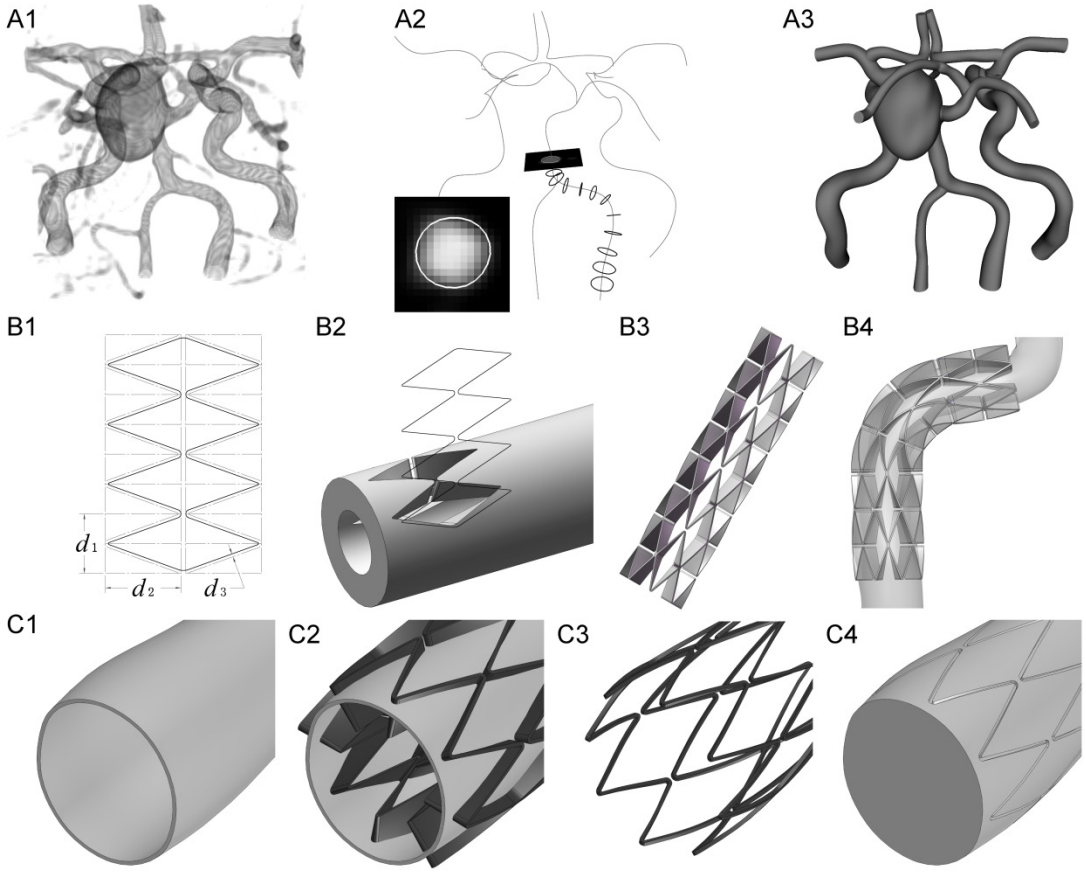

Figure 2.1: Method of patient-specific model construction. Imaging data, shown as a volume rendering (A1), is used to generate vessel centerlines and 2-D segments of the arterial geometry (A2). The segments were lofted together to create a 3-D solid model (A3). A parameterized sketch of the stent cell (B1) is wrapped around a thick tube (B2) and propagated along the length of the tube to create model of a thick stent (B3). The thick stent is flexed to match the arterial geometry (B4). The solid vessel (C1) is hollowed to radial thickness equal to that of the stent, such that the intersection of the thick model of the stent and thin vessel (C2) yields a patient-specific stent (C3) that is subtracted from the solid model to produce the flow domain (C4).

2.2.2 Creation of stent models

The approach discussed below requires knowledge of the expanded orientation of strut linkages. If not known, this information can be determined in a number of ways

including performing FEA for a portion of the stent [83, 113] or deploying a stent and quantifying the orientation of its strut linkages using light microscopy or microfocal x-ray computed tomography [83, 91]. A CAD drawing of the expanded stent pattern is then created. The drawing is constrained using a set of equations and other criteria that allow the user to easily control specific features of the model (Figure 2.1: B1). This parametric approach allows for properties including the number, width and circumferential or longitudinal spacing (i.e. scaffolding) of struts, as well as the implantation diameter and stent length, to be easily adapted using variables. The drawing, and subsequent stent model, can then automatically be regenerated for rapid parametric analysis of the contribution of these design properties to resulting hemodynamic alterations.

The drawing of the expanded stent is wrapped around a tube with a diameter slightly larger than the vessel in which the stent will be virtually implanted and a thickness >5-times the desired stent thickness. The cell geometry of the stent is then cut out of the tube, resulting in a stent design that accurately represents a commercially available stent with an accentuated radial thickness (Figure 2.1: B2-B3). Each stent design in this study was created using CAD software capable of saving a Parasolid document such as Solidworks (Solidworks Corp., Concord, MA) or SolidEdge (Siemens, Plano, TX) in order to facilitate integration of the vessel and stent models.

2.2.3 Virtual stent implantation

Virtual stent implantation is achieved using a series of Boolean operations. The thick stent is flexed to match the curvature of the vessel (Figure 2.1: B4). A separate solid model of the vessel to undergo virtual stenting is created and hollowed to the desired stent thickness (Figure 2.1: C1). A Boolean intersection operation is then performed with

the hollowed vessel and thick stent to yield a computational representation of the stent to undergo virtual implantation (Figure 2.1: C2-C3). Then a Boolean subtraction operation is performed with this stent and the patient-specific model in order to remove the stent from the lumen and generate the flow domain for CFD analysis (Figure 2.1: C4). In the presence of branching arteries, the Boolean intersection that yields the patient-specific stent is performed only on the main vessel, with any branching arteries removed from the model. The subsequent subtraction of the patient-specific stent is performed on the entire model of the vasculature such that the struts of the stent partially occlude the branching arteries.

2.2.4 Specification of CFD boundary conditions and simulation parameters

Boundary conditions varied slightly between applications and specific details unique to each vascular bed will be presented in the subsequent examples. Generally, inlet boundary conditions were obtained from experimental data [33, 57] and outlet boundary conditions that replicate measured blood flow and pressure were applied. To replicate the physiologic influence of vessels distal to CFD model branches, a three-element Windkessel representation was imposed at model outlets using a coupled-multidomain method [112]. The three-element Windkessel method provides a good estimate of the arterial tree beyond model outlets [105] and can be described by three main parameters with physiologic meaning: R_c, C and R_d. R_c is the characteristic impedance representing the resistance, compliance and inertance of the proximal artery of interest, C is the arterial capacitance and represents the collective compliance of all arteries beyond a model outlet, and R_d describes the total distal resistance beyond a given

outlet. The procedure for calculating the Windkessel parameters at each outlet is as follows:

1) Compute the total resistance (R_t) for the entire model based on mean blood pressure (BP) and flow (Q) measurements. Note that $BP=Q*R_t$.
2) Estimate the total arterial compliance (TAC) for the entire model from measured inflow and BP measurements using the pulse pressure method [105]. Assume a R_c:R_t ratio of 6%, where $R_t= R_c+R_d$ [65].
3) Distribute TAC and R_t among the model outlets according to the blood flow distribution to the outlets. Tune the R_c:R_t ratio at each outlet using the pulse pressure method thereby replicating the desired BP values at each outlet [105].

Blood was assumed to behave as a Newtonian fluid with a density of 1.06 g/cm^3 and dynamic viscosity of 4 cP. Three or four cardiac cycles were run to ensure simulation results were converged with a maximum error between equivalent time points in successive cardiac cycles <1 mmHg and 1 mm^3/s for pressure and flow, respectively. The simulation time-step was chosen for a Courant, Friedrichs and Lewy condition <1. Simulations were also scrutinized to ensure results were independent of the number of mesh elements in each model. Anisotropic meshes were created with unstructured tetrahedral elements using a commercially available, automatic mesh generation program (MeshSim, Simmetrix, Clifton Park, NY). Initial meshes were generated such that the density of elements around the stent struts was much greater than throughout the rest of the model. Meshes were further adapted after each pulsatile simulation to place more elements near struts and other regions where they are most needed within the flow domain while inserting fewer elements where a coarse density is sufficient [84]. The

desired mesh independence criteria strived for a change in time-averaged WSS values <0.1 dynes/cm^2 at predetermined proximal and distal intrastrut regions between successive meshes [56, 87]. Simulations were performed using a stabilized finite element method to solve equations for conservation of mass (continuity) and balance of fluid momentum (Navier-Stokes). Vessel wall elastodynamics equations were also solved in cases where a deformable model was used to define the vessel wall[112].

2.3 Simulation quantification methods

The following portion describes the post-processing techniques for quantifying and visualizing hemodynamic indices associated with stent performance. While they are presented as a general set of quantification methods, these techniques may not be applicable to all stenting scenarios. For example, the turbulent kinetic energy described below is often quantified in aneurismal geometries, but it would not be investigated in a study of coronary stents where flow is largely laminar.

2.3.1 TAWSS, OSI and displacement computation and visualization

After verifying that simulation results were mesh independent and replicated aimed BP and flow distributions, time-averaged wall shear stress (TAWSS) and oscillatory shear index (OSI) were computed over the last cardiac cycle as previously described [108]. Specifically, TAWSS was computed at each node on the surface of the CFD mesh as:

$$TAWSS = \left| \frac{1}{\mathrm{T}} \int_0^{\mathrm{T}} \overrightarrow{WSS}\, dt \right|$$

where $\overrightarrow{WSS}$ is the WSS vector at a node and T is the period of one cardiac cycle. Similarly, OSI was computed at each surface node as:

$$OSI = \frac{1}{2}\left(1 - \frac{\left|\frac{1}{T}\int_0^T \overrightarrow{WSS}\, dt\right|}{\frac{1}{T}\int_0^T \left|\overrightarrow{WSS}\right| dt}\right)\overrightarrow{WSS}$$

OSI is a measure of the directionality of WSS in which lower OSI values indicate WSS is oriented predominately in the primary direction of blood flow while a value of 0.5 is indicative of bi-directional WSS with a time-average value of zero throughout the cardiac cycle.

In cases where the model walls were defined as a deformable surface, the maximum circumferential strain (ϵ) was computed as:

$$\epsilon = \frac{c_{sys} - c_{dia}}{c_{dia}}$$

where c_{sys} and c_{dia} represent the vessel circumference during systole and diastole. The circumference was measured at a vessel cross-sections perpendicular to the vessel centerline.

2.3.2 Unwrapping the vessel surface geometry

To better visualize TAWSS, or other relevant hemodynamic indices at the vessel wall, the surface geometry of a vessel was unwrapped whereby each (x, y, z) node of the surface mesh was mapped to a (θ, l) coordinate system. The dimension θ represents the angular position of the node for 0-360 degrees in which the zero degree location was arbitrarily chosen, but most often selected to lie along some convenient landmark such as the inner or outer curvature of a vessel. The dimension l represents the length along the vessel in which the node was located.

The length along the vessel was measured relative to the centerline of the vessel. Unfortunately, the centerline path created when modeling the vessel geometry from the imaging data (Figure 2.1: A1) could not be used to unwrapped the surface geometry because it was a user-created path and may not accurately represent the center of the vessel. Since θ is measured relative to the centerline, an off-center path would distort the θ measurement (Figure 2.2). It was therefore necessary to create an unbiased centerline path to unwrap the vessel surface geometry.

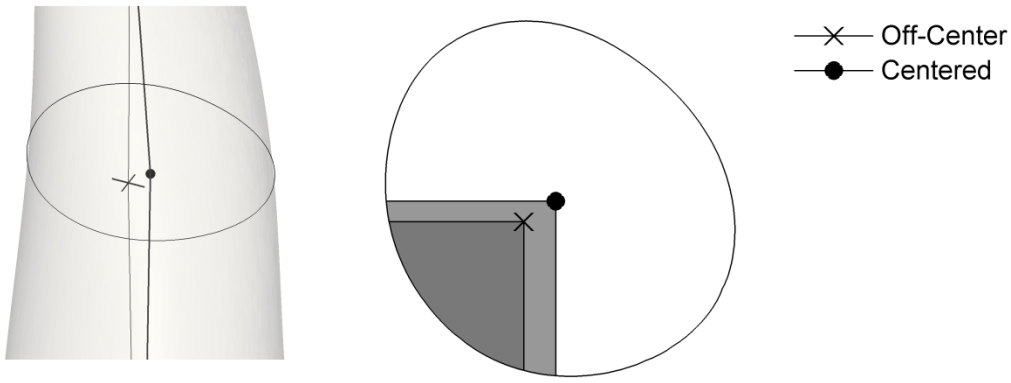

Figure 2.2: Comparison of θ quantification with using an off-center and a centered vessel path. (Left) A 3D representation of the vessel and the two paths. (Right) Cross-section of the vessel with path/plane intersections of the paths denoted. A 90° section of the vessel wall is denoted with within the gray shaded areas originating from the two paths. Note that the extent of the vessel wall included within the 90° section differs depending on the location of the centerline.

The corrected path was computed using the original, or model construction, path as a guide. The model construction path was traversed and planar cross-sections of the vessel surface mesh were computed at regular intervals. The center of each cross-section was calculated as the center of an algebraic least-squares fit of a circle [34]. The computed centers of each cross-section were then used to construct the corrected path. Initially, it was proposed the centroid of the cross-section could be used as the center of

the cross-section. However, using the centroid caused the correct path to be skewed away from bifurcating vessels (Figure 2.3), thus a circle fitting algorithm was adopted.

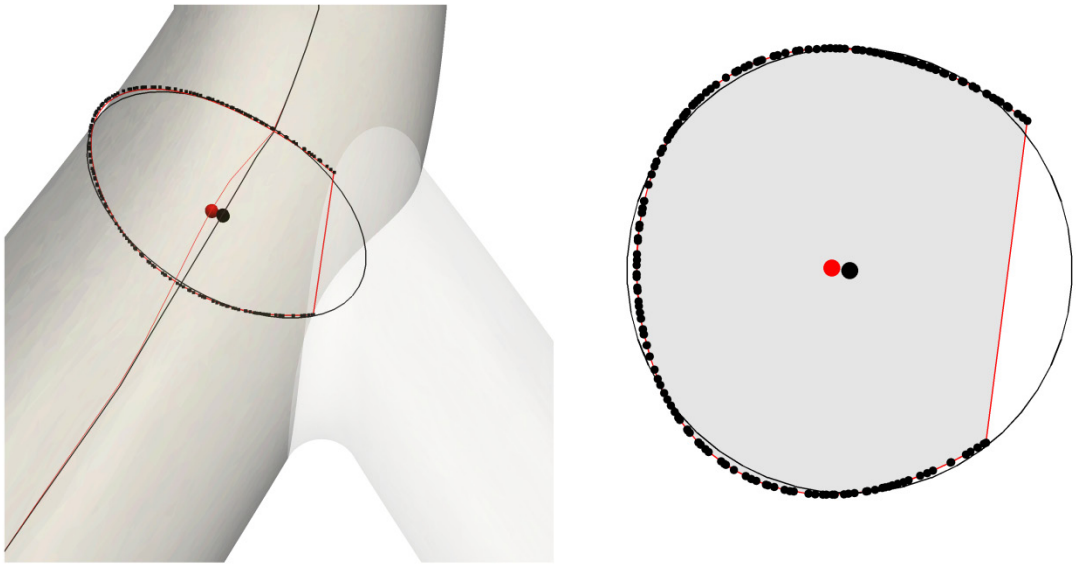

Figure 2.3: Comparison of algorithms for computing the centerline of a vessel at a bifurcation. (Left) 3D representation of the bifurcation and the centerline path computed using the centroid (red) and circle-fitting (black) algorithms. (Right) Cross-section of the main vessel at the bifurcation. The centroid (red dot) of the vessel is computed using the area shaded in gray. Because the branching vessel is removed during the analysis, the centroid is skewed away from branch location. The center of the fitted circle (large black dot) was computed using the points from the surface of the main vessel geometry (small black dots). Note that the fitted circle (black line) provides a good approximation of the center of the vessel even when a large portion of the vessel cross-section is removed.

The corrected path was then used as the reference from which l was computed for each node of vessel surface geometry. A *Frenet-Serret* frame was used to define a local coordinate system along the centerline of the vessel. This moving coordinate system consisted of a tangent (T), normal (N) and binormal (B=T×N) vector as shown in Figure 2.4. Using this coordinate system, l was defined for each node as the length along the centerline where the surface mesh node intersected the plane defined by the normal and binormal vector (NB-plane). The distance (d) between a mesh point (p_m) and the NB-plane was given by:

$$d = T(l) \cdot p_m - T(l) \cdot p_c(l)$$

where p_c is the point along the centerline at some length l. The length l along the centerline for each mesh point was determined by setting d=0 and solving the remaining equation. However, this was not a trivial computation since it is dependent on the definition of $T(l)$ and $p_c(l)$. The simplest method to define T and p_c is using piecewise linear interpolation between the points of the corrected centerline, but this results in somewhat uneven vessel mapping due to the discontinuities at each point of the centerline. For smoother mapping, piecewise Hermite cubic spline interpolation was used as it provides C^1 continuity at each point of the centerline [82].

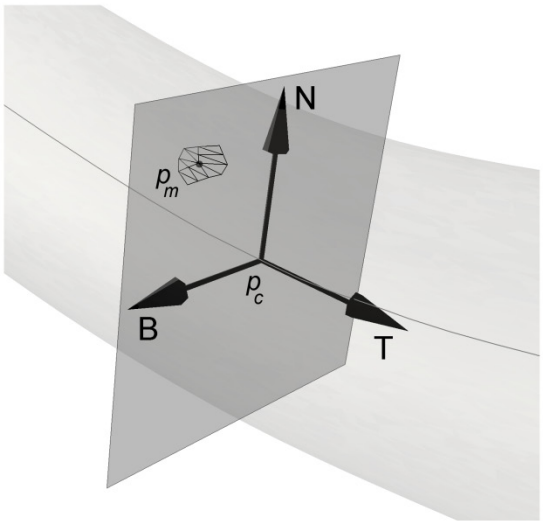

Figure 2.4: Moving coordinate system used when computing the distance, or length, along the centerline path for a point on the surface mesh of the vessel.

The last step to unwrapping the surface geometry of a vessel was computing the angular position, θ, relative to the center for each point on the surface mesh. This calculation was performed in the NB-plane. One option for computing angular position was to calculate the angle between the vectors $(p_m - p_c)$ and N, where N is defined as the 0° position. However, when using a *Frenet-Serret* frame, N is always directed towards the center of the curvature which causes erratic orientation changes, or twisting of the 0°

position. For the purposes of visualizing hemodynamic parameters, it is more desirable to use the parallel transport method [17, 37] to minimize the amount of twisting of the reference 0° position. Thus, θ was calculated at each point on the surface of vessel geometry as the angle between the vectors $(p_m - p_c)$ and a parallel transport vector (Figure 2.5).

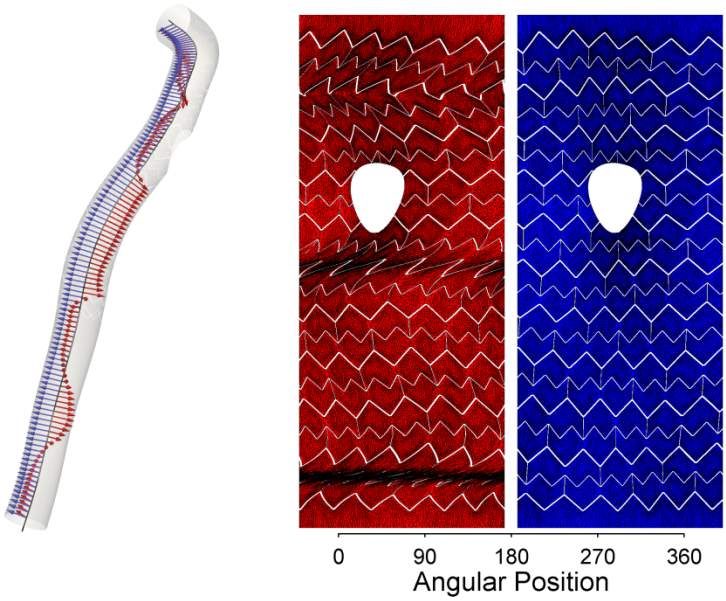

Figure 2.5: Comparison of methods for computing the angular position when unwrapping a vessel geometry. (Left) The 3D vessel geometry of a stented coronary artery. The vessels centerline path is shown along with the vectors indicating the 0° position computed using the Frenet-Serret coordinate system (red) and the parallel transport method (blue). (Right) Resulting unwrapped vessel computed using the Frenet-Serret coordinate system (red) and the parallel transport method (blue). The difference between the methods is shown using a stented vessel as the stent struts illustrate the amount of twisting associated with each method.

2.3.3 Computing mean exposure time

Flow stasis was quantified by computing mean exposure time (MET), recently defined by Lonyai *et al*. [71]. Using a particle tracking scheme, MET measures the duration massless particles reside within in each element of an MET mesh. In the stented models of this investigation, the mesh adaption process created highly anisotropic meshes

with more elements along the stent struts, which was not suitable for computing MET. Auxiliary isotropic meshes were therefore used as part of a post-processing step for the MET calculations since this index depends on element size. To calculate MET for an element *e*, N_e is defined as the number of times a particle passes through the element, V_e as the volume of the element, N_t as the total number of particles released, and $H_e^p(t)$ as equal to 1 when a particle *p* is located inside the element at time *t* and is equal to 0 otherwise such that the MET is given by:

$$MET = \frac{1}{N_e {V_e}^{1/3}} \sum_{p=1}^{N_t} \int_0^{\infty} H_e^p(t) dt$$

Because the duration a particle resides within an element (i.e. the summation on the right side of the MET equation) is normalized by the N_e, MET distinguishes between recirculating particles and stagnant particles unlike other flow stasis measurements that quantify a cumulative duration. For example, if the duration a particle spends in an element is equal to 1.0 second and the particle encountered the element once, the computed MET would be higher than a recirculating particle that passes through the element twice whose cumulative duration within the element was 1.0 second. In this manner, flow stagnation is weighted higher than recirculation when computing MET.

In the previous study of MET around venous pacemaker leads, Lonyai *et al*. also normalized the duration a particle resides within an element to V_e [71]. In this investigation the duration a particle resides within an element was instead normalized to ${V_e}^{1/3}$, since it was noticed that variations in element size can result in large variations in MET if normalized to V_e, as illustrated in Figure 2.6. Given the relatively small element size of the auxiliary meshes used in this investigation, it could be assumed particle

movement through the elements was highly one-dimensional, and normalizing the duration a particle resides within an element to $V_e^{1/3}$ reduced variations in MET resulting from differences in element volume.

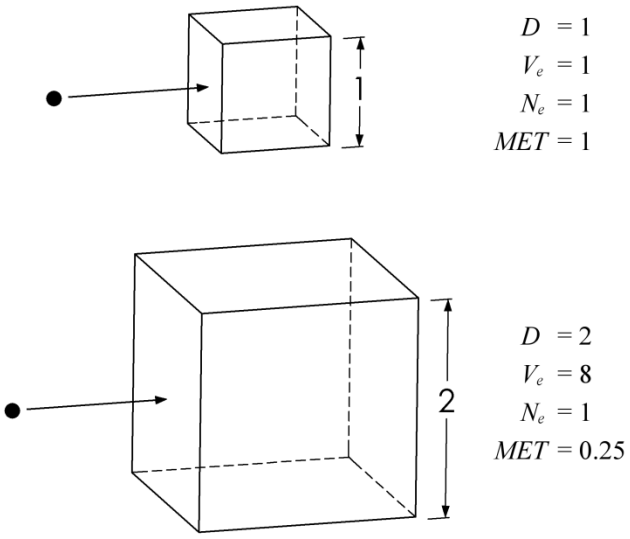

Figure 2.6: A simple example of the variation in mean exposure time (MET) caused by differences in element size. A particle moving with a velocity = 1 is shown passing through a small cubic element (top) and a cubic element with an edge size twice as large (bottom). It is assumed the particle passes through each element once (N_e=1) with a one-dimensional trajectory, such that the duration (D) the particle resides in the element is proportional to the edge size. Using the MET definition of Lonyai *et al*., $MET=D/(N_eV_e)$, the computed MET differs between the elements due to the large variation in the volume of the element (V_e). Applying the MET definition used in this investigation, $MET=D/(N_e V_e^{1/3})$, results in a computed MET of 1 for each element.

The results of the MET analysis may be sensitive to the strategy with which particles are released. There are two primary methods for seeding the computational domain, uniformly seeding the entire model or seeding just the inlet. Uniformly seeding the entire domain ensures particles populate all regions of the model, but it is likely that proximal regions of the model will not encounter as many particles as the distal regions. In contrast, seeding the inlet of the model ensures both the proximal and distal regions of the vasculature encounter an equal number of particles, but there is the potential that

particles would not populate areas of slow or recirculating flow. To overcome the disadvantages of both release strategies, a hybrid release strategy was used in which an initial uniform seeding of the entire model was supplemented with particles released from the inlet of the model over the course of one cardiac cycle. The inlet particles were released in a fashion uniform with respect to both space and time such that a greater number of particles were released in high velocity areas, shown in the simplified example in Figure 2.7. After one cardiac cycle, the inlet release was ceased, and the MET analysis was continued for additional cycles until all the particles exited the domain.

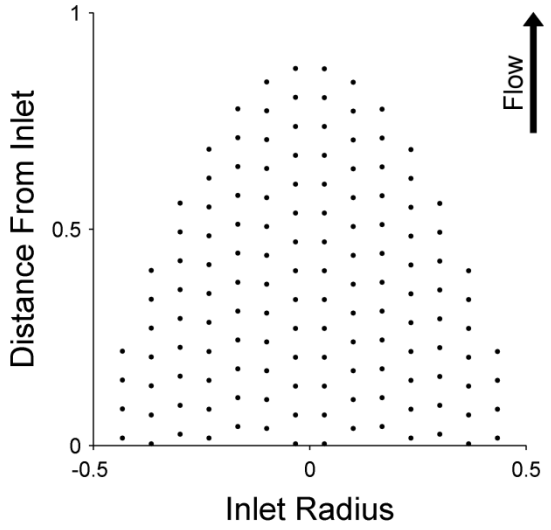

Figure 2.7: A simple, two-dimensional example of a particle release into steady flow at the inlet of an ideal tube. Particles are shown as being released from the inlet (diameter = 1) at uniformly spaced locations (spacing = 0.1). The timing of the particle release is computed such that additional particles are released at each location in a similarly uniform fashion.

In addition to the particle release strategy, the density of particles released likely influences the results of the MET analysis as well. To analyze the effect of particle density, MET analyses with different particle densities were performed for both the coronary and cerebral stenting applications. In each case, the first analysis was performed with about 1.5 million particles, followed by a second analysis with about 3 million

particles and third with about 6-7 million particles. To examine the effect of particle density within the entire geometry, a histogram, or discrete probability density function (PDF), was computed to characterize the distribution of MET for both the low, medium and high particle density MET computations. The PDF bin size was 0.0025 s/cm over a range of 0 to 0.4 s/cm. For both the coronary and cerebral applications, a bin to bin comparison of the MET histograms revealed a maximum difference >20% between the low and medium particle density MET computations but a maximum difference <2.5% between the medium and high particle density releases. Thus, MET computations performed with 3 million particles were assumed to adequately resolve the MET field, but the results of the high density releases are reported in the subsequent examples given that these results were already computed for this analysis.

To facilitate several MET analyses with a large number of particles, the MET code was ported to a computer cluster and parallelized to improve the speed of the analysis. Unlike the parallel CFD solver, the MET code was not parallelized by splitting up the model geometry. Instead, the entire model and CFD results were distributed to each processor and the particle release was split among the processors. This parallelization strategy was chosen to minimize the amount of data transferred between the processors. This is best illustrated with a simple example. Consider an MET analysis split up among five processors. Each processor would receive a copy of the CFD results but would only be assigned about 1/5 of the particles. After each processor completes its analysis, the computed MET for each processor is combined on an element by element basis to produce the complete MET analysis. This parallelization strategy is most efficient when the number of particles assigned to each processor is equal. Since the

speed of the MET code on one processor is proportional to the number of particles released, an uneven distribution causes processors with a greater number of particles to create a bottleneck for the entire analysis. For this reason, it is not efficient to parallelize the particle release based on time (e.g. Five processors, each processor advects the particles released during 1/5 of the cardiac cycle), because more particles would be assigned to processors that analyze systole than those that analyze diastole. As shown in Figure 2.8, distributing the particle release among the processors based on flow rate results in an equal and more efficient distribution of particles among the processors.

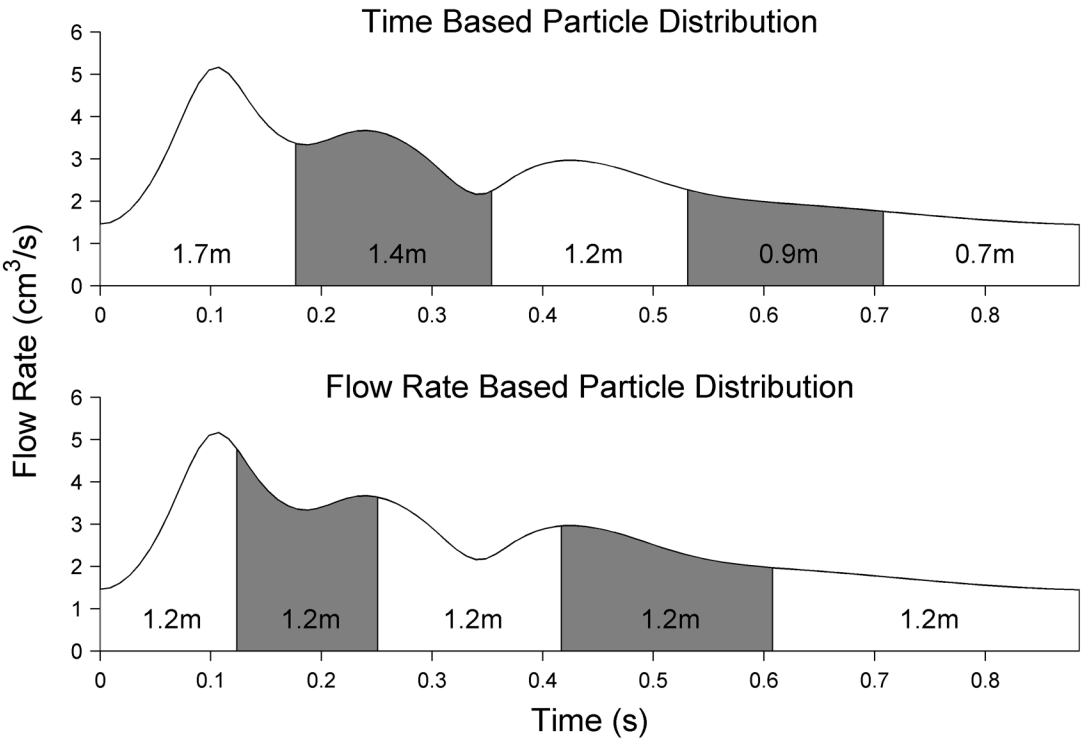

Figure 2.8: An example of time based and flow rate based strategies for distributing the particle release among multiple processors to compute MET. In this example, the release of six million particles over one cardiac cycle is distributed among five processors. The portion of the particle release assigned to each processor is denoted by the alternating gray and white areas under the flow waveform. The number of particle assigned to each processor is also denoted (in millions).

2.3.4 Computing turbulent kinetic energy

Turbulence was quantified as the cycle-to-cycle variation within the velocity field as previously described [95]. Once simulations were considered converged, four more cardiac cycles were simulated, resulting in five well-converged cycles. An ensemble-averaged velocity for each time point within the cardiac cycle was then computed over the last five cycles. Subtracting the ensemble-averaged cycle from the original velocity field results in the fluctuating component of the velocity, $\vec{\tilde{u}}(\vec{x}, s)$. Mathematically, the fluctuating velocity field can be used to compute the turbulent kinetic energy as:

$$TKE(\vec{x}, s) = \frac{1}{2}\rho[\langle\tilde{u}_1^2\rangle(\vec{x}, s) + \langle\tilde{u}_2^2\rangle(\vec{x}, s) + \langle\tilde{u}_3^2\rangle(\vec{x}, s)], \forall s \in [0,T)$$

where *T* is the period of the one cardiac cycle, ρ is the density of blood, $\tilde{u}_1$, $\tilde{u}_2$, and $\tilde{u}_3$represents the *x, y,* and *z* components of the fluctuating velocity, and $\langle\tilde{u}\rangle(\vec{x}, s)$ denotes an ensemble average of a fluctuating velocity component. Similarly, the ensemble-averaged kinetic energy (KE) is computed as:

$$KE(\vec{x}, s) = \frac{1}{2}\rho[\langle u_1^2\rangle(\vec{x}, s) + \langle u_2^2\rangle(\vec{x}, s) + \langle u_3^2\rangle(\vec{x}, s)], \forall s \in [0,T)$$

where u_1, u_2, and u_3 represents the *x, y,* and *z* components of the ensemble averaged velocity. Finally, the ratio of TKE\KE was computed at peak systole.

2.4 Case Study 1: Comparing the hemodynamic alterations between stents after virtual implantation across a coronary bifurcation

In the coronary vasculature, the stenting of bifurcation lesions, which accounts for 15-20% of treated lesions, is associated with high rates of restenosis and thrombosis [44, 98]. To date the majority of bifurcation stenting studies has analyzed the effects of various single and multiple stenting strategies. Because a large emphasis has been placed

on the stenting technique, very little is known about the potential influence of stent design when used to treat bifurcations. Thus, the objective of the case study was to apply the virtual stenting method to characterize the hemodynamic differences between two stent designs placed across a bifurcation. It should be noted that the predominant bifurcation stenting technique is main vessel stenting with provisional side branch stenting [103], which results in the presence of stent struts across the ostium of the side branch. For this reason, both the local hemodynamics within the main vessel and side branch need to be considered when examining the hemodynamic performance of each stent.

2.4.1 Methods

A CFD model was created as described above from computed tomography data obtained from the OsiriX medical imaging repository (http://pubimage.hcuge.ch:8080/). The patient did not have a significant stenosis and the left anterior descending (LAD) and first diagonal branch diameters, branch angle and radius of curvature matched published normal values [30, 90]. Computational representations of an open-cell ring and link design (Stent A) and a close-cell slotted tube prototype design (Stent B) created through contract manufacturing for use with experimental investigations were virtually implanted using the methods described above (Figure 2.9). The resulting stented vessels mimicked the clinical practice of main vessel stenting without subsequent side branch balloon angioplasty.

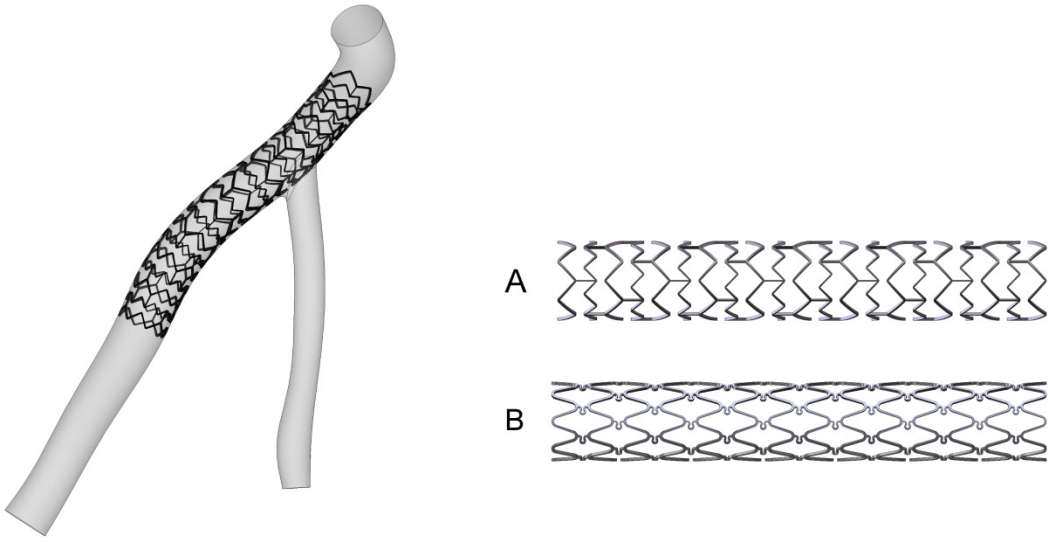

Figure 2.9: Coronary model in which an open-cell ring and link, Stent A, and a closed-cell slotted-tube, Stent B, design were virtually implanted.

An LAD blood flow waveform at rest [56] was applied at the model inlet. At the outlets, the three-element Windkessel was applied, although in the coronary vasculature the Windkessel parameters are difficult to compute as ventricular contraction causes time-varying changes in resistance [53]. Van Huis *et al*. demonstrated that the in the absence of ventricular contraction the system can be assumed as linear, and the zero hertz impedance, Z_0, is between 22-65% less than the total resistance [111]; therefore the total resistance total resistance (R_t), was scaled by 65% to fall with this range. The characteristic impedance (R_c), was calculated from the pulse wave velocity of coronary arteries as [111]:

$$R_c = \frac{\rho \cdot c_{ph}}{\pi r^2}$$

where ρ is the density of blood, c_{ph} is the arterial pulse wave velocity, and r is the artery radius. A pulse wave velocity of 8.6 m/s was used in this investigation [5]. Given, R_c and the scaled R_t, the arterial capacitance parameter was computed as described earlier to

replicate the desired BP. At the vessel wall, the stent was modeled as rigid while the vessel was modeled as deformable. The modulus of elasticity and thickness of the vessel wall were selected to match the deformation previously observed during resting flow conditions [89].

Previous studies have demonstrated that distributions of TAWSS <4 dyn/cm^2 and high temporal oscillations in WSS quantified by OSI are associated with cellular proliferation, intimal thickening and inflammation [39]. In addition to unwrapping the vessel geometry to visualize these hemodynamic parameters, the area of the stented region exposed to TAWSS <4 dynes/cm^2 and the area of the lumen surface containing OSI >0.1 were quantified. Due to differences in intrastrut area (i.e. scaffolding) and the number of strut linkages between the similarly sized stents, TAWSS and OSI were normalized to the overall area of the stent interfacing with the luminal wall. Vessel wall strain was quantified within each intrastrut area at the point of the largest wall displacement. MET was computed at the bifurcation to visualize flow stasis in both the main and side branches induced by stent placement.

2.4.2 Results

Two stented models and a corresponding unstented model of a coronary bifurcation were created using the described method of stent implantation. The stent creation and implantation into the previously built vessel geometries was accomplished in 12-16 hours for each coronary stent. CFD simulations of the final stented coronary meshes (3.2 million elements) took about 2.9 hours per cardiac cycle, whereas the unstented coronary geometry (2.2 million elements) took 1.75 hours per cardiac cycle.

Distributions of TAWSS in the coronary arteries for the two stent types are illustrated in Figure 2.10. The main branch stent struts induced non-uniform distributions of WSS in the side branch immediately distal to the stent (Figure 2.10, epicardial and myocardial inserts). Regions of low TAWSS (<4 dynes/cm^2) were localized near the struts and more prevalent distal to the bifurcation in both stent models. The total intra-strut area of the lumen exposed to low TAWSS was higher for the open-cell ring-and-link design (Stent A) (75.6%) than the close-cell slotted-tube design (Stent B) (59.3%). The curvature of the model caused localized areas of low TAWSS along the myocardial side of the LAD lumen in both models. Analysis of the unstented model (results not shown) revealed the amount of lumen exposed to low TAWSS due to native vessel geometry is 5.8%, thus the amounts of stent-induced low TAWSS are 69.8% and 53.5%. There were only modest differences in the area of the luminal surface exposed to high OSI between the two stent models (<1% for both models), but localized areas of high OSI were found to correspond to areas of low TAWSS along the myocardial lumen surface just distal to the bifurcation.

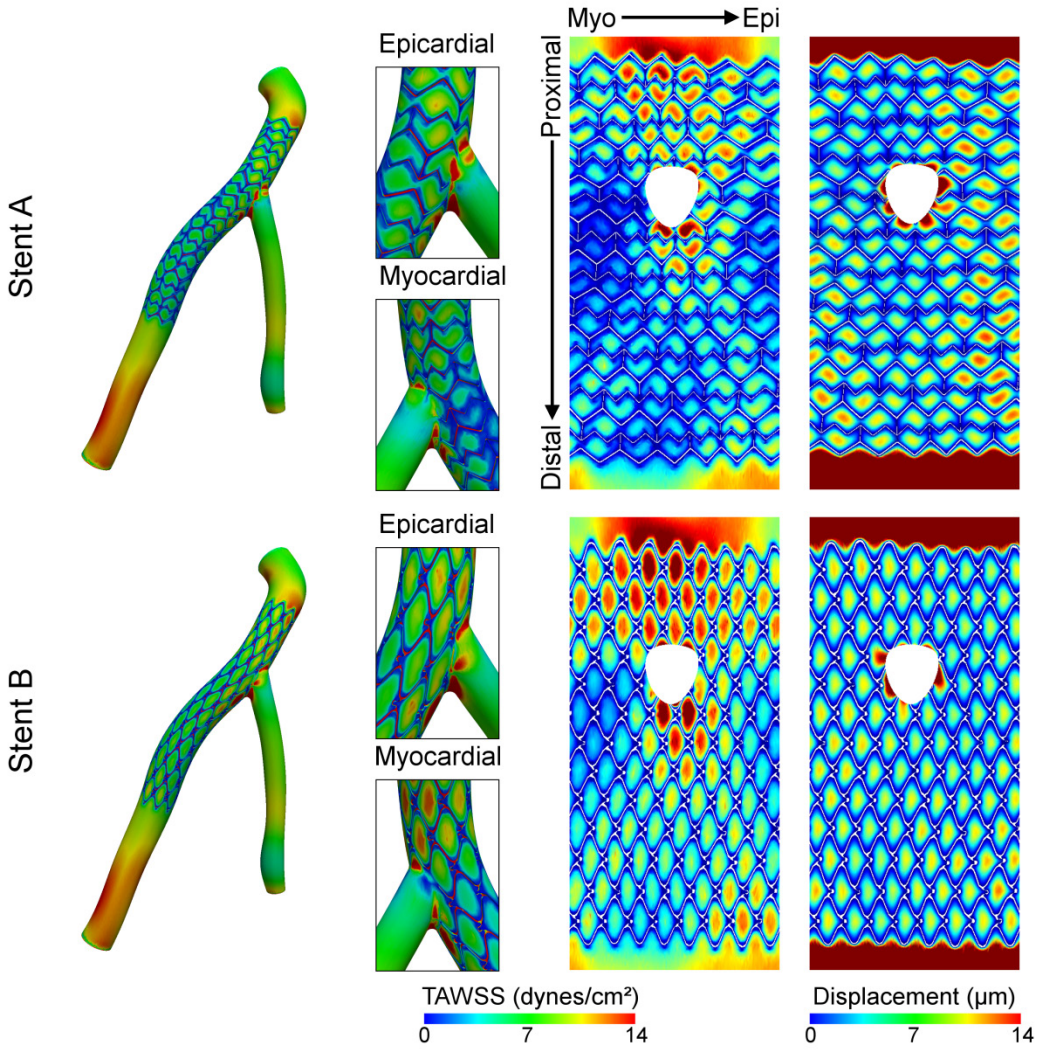

Figure 2.10: Comparison of hemodynamic indices between coronary Stent A and Stent B. Time-averaged wall shear stress (TAWSS) is shown on the vessel (left) and the inserts show the distribution at the bifurcation as a result of partial side branch occlusion. The main branch of the vessel was unwrapped to visualize intrastrut TAWSS and vessel wall displacement.

Displacement of the wall in the intrastrut region was ten times less than that in other portions of the LAD (Figure 2.10). The larger open-cell geometry of Stent A allowed for a greater intrastrut peak displacement. However, the closed-cell design of Stent B allowed for a greater average circumferential wall strain due to the pattern of wall

deformation within the intrastrut region (0.0035 vs. 0.0040). These values were much less than the strain of vessel wall distal to the stent which was near 0.03.

Approximately 6.2 million particles were released in each bifurcation model over the course of one cardiac cycle and tracked for an additional 19 cardiac cycles to compute MET. Figure 2.11 illustrates several cross-sections of the MET field (computed with 6.2 million particles) near the bifurcation. Stent implantation increased the region of high MET near the wall of the vessel in the main branch (Figure 2.11, bifurcation plane and cross-section A). The most pronounced difference in MET due to stent implantation was in the side branch, just distal to the stent (Figure 2.11, cross-section B). In this region, the MET mimicked the stent design, placement, and number of struts in the side branch which caused MET near the center of the vessel to increase relative to the unstented model. Approximately 1.25 mm distal to cross-section B the MET field of the stented models reflected that of the unstented model, with only slight differences in area of high MET near the vessel wall. The MET was lowest near the carina of the bifurcation which corresponds to increased velocity in this region.

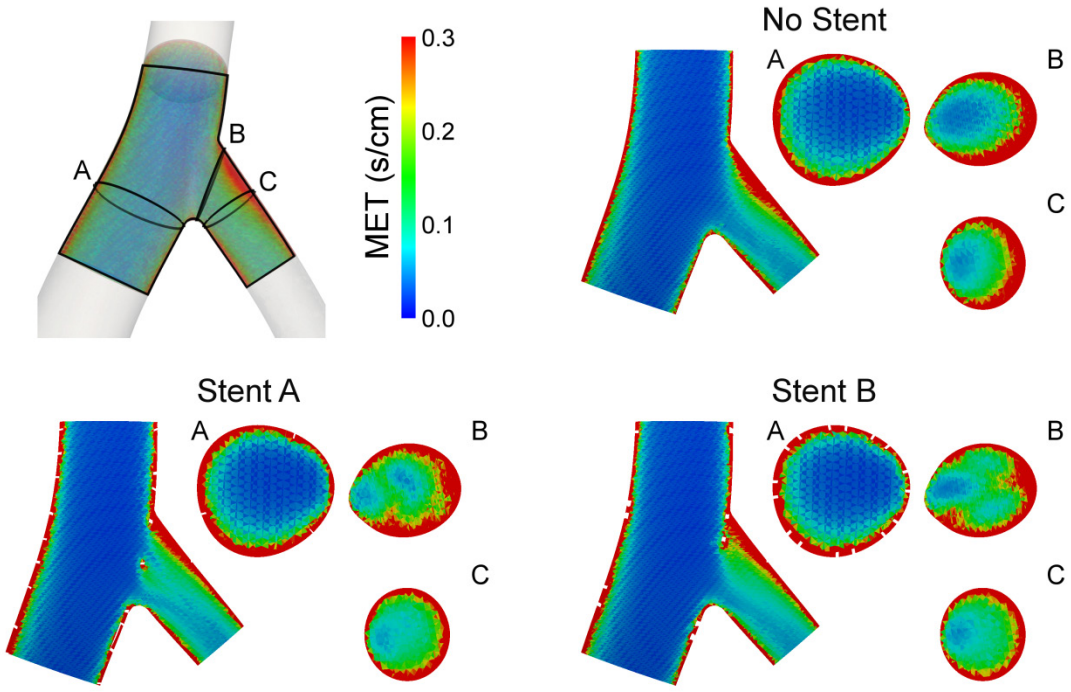

Figure 2.11: Cross-sections of the mean exposure time (MET) at the coronary bifurcation for one unstented and two stented models. MET is visualized in a plane parallel to the bifurcation and three planes perpendicular to the vessel (top, left). The two planes in the side branch of the bifurcation (B-C) are separated by a centerline distance of approximately 1.25 mm.

2.4.3 Discussion

Several properties of coronary stent design influence local hemodynamics within the coronary vasculature, such as strut size, width, deployment ratio, etc [60, 93]. In this study, the area of low WSS, an indicator for the localization of neointimal hyperplasia and subsequent restenosis, was determined to be greater for the open-cell ring-and-link design (Stent A). Since strut radial thickness and deployment ratio were kept constant for both stent designs, the higher WSS of the closed-cell slotted-tube design (Stent B) is likely the result of a longitudinal stent strut angle which is more aligned in the primary blood flow direction [62].

Using circumferential strain as a measure of the wall motion, Stent B allowed for slightly more wall motion than Stent A. Although somewhat counter-intuitive since initial visual inspection of calculated wall displacement indicated Stent A had higher peak displacement, the longer longitudinal length of the stent cell geometry of the prototype stent allows for a greater amount of strain to be generated in intrastrut regions. It should be noted the vessel was modeled with a constant compliance throughout the geometry, but compliance may vary spatially due to the presence of atherosclerotic lesions.

MET in the side branch just distal to the coronary stent is highly influenced by both the stent design and stent position (Figure 2.11, cross-section B), and it is difficult to predict which stent design performs best. Interestingly, the difference in MET due to struts crossing the side branch is quite diminished 1.25 mm distal to the stent (Figure 2.11, cross-section C), and it is unknown if the small volume of high flow stasis within this region is hemodynamically significant. While the effects of stent position were not considered in this investigation, Williams and Koo *et al*. modeled a worst case and best case stent position across the side branch in an ideal model and observed minimal changes in hemodynamics between the models [117]. Still, additional studies are needed to better understand the effects of the stent position on disease progression within stented bifurcations. The method of stent implantation demonstrated in this investigation is well-suited for investigating stent positions due to the control the user has during stent placement.

2.5 Case Study 2: Quantifying the effect of stent strut size on cerebral aneurysm hemodynamics

Cerebral aneurysm rupture is the second leading cause of stroke in the United States [69]. To avoid rupture, blood flow to an aneurysm can be occluded to promote flow stagnation and induce thrombosis by means of surgical clipping or endovascular devices including coils and stents. In saccular aneurysms, coiling has been shown to be an effective treatment for rupture prevention [79]. Wide-necked aneurysms are more difficult to treat, and often a stent is used in conjunction with coiling to facilitate thrombosis in these cases [97, 114]. Stent porosity, strut size, and cell geometry have all been identified as factors that affect cerebral stent performance [12, 52]. Decreased strut size of helical stents has been shown to favorably alter flow in idealized aneurysms geometries using particle image velocimetry (PIV) [68]. The objective of this example was to evaluate how the strut size of stent designs similar to the commercially available Neuroform2 stent (Boston Scientific Neurovascular, Fremont, CA) affects hemodynamics in a patient-specific model of a wide-necked aneurysm using the computational stenting methods described above.

2.5.1 Methods

A cerebral model of a patient with a large basilar trunk aneurysm was constructed from magnetic resonance imaging data also obtained from the OsiriX medical imaging repository. Three stent designs similar to the Neuroform2 were modeled in an expanded configuration using the parametric modeling techniques described earlier (Figure 2.12). All stents had the same porosity but their strut size was varied for use in three CFD simulations. The number of longitudinal and circumferential repetitions was increased as

stent strut size decreased in order to maintain a constant porosity in each model as shown by the design specifications in Table 2.1. Though these stents are often used in conjunction with coils, only a stent model was placed across the neck of the aneurysm in order to isolate and characterize stent performance.

Unlike the coronary stenting case study, both the stent and vasculature were assumed to be rigid. Time-varying waveforms were imposed at the model inlets (2 vertebral and 2 internal carotid arteries) based on previously characterized flow waveforms in this area of vasculature [33]. Three-element Windkessel model representations were prescribed at the six outlets of the model (2 anterior, 2 middle, and 2 posterior cerebral arteries) to match the flow distribution in the Circle of Willis [107].

Table 2.1: Design parameters for three cerebral stents with a constant porosity.

Stent Abbreviation	Longitudinal Repetitions	Circumferential Repetitions	Strut Width (μm)
N2-8x8	8	8	93.7
N2-10x12	10	12	73.4
N2-12x16	12	16	65.0

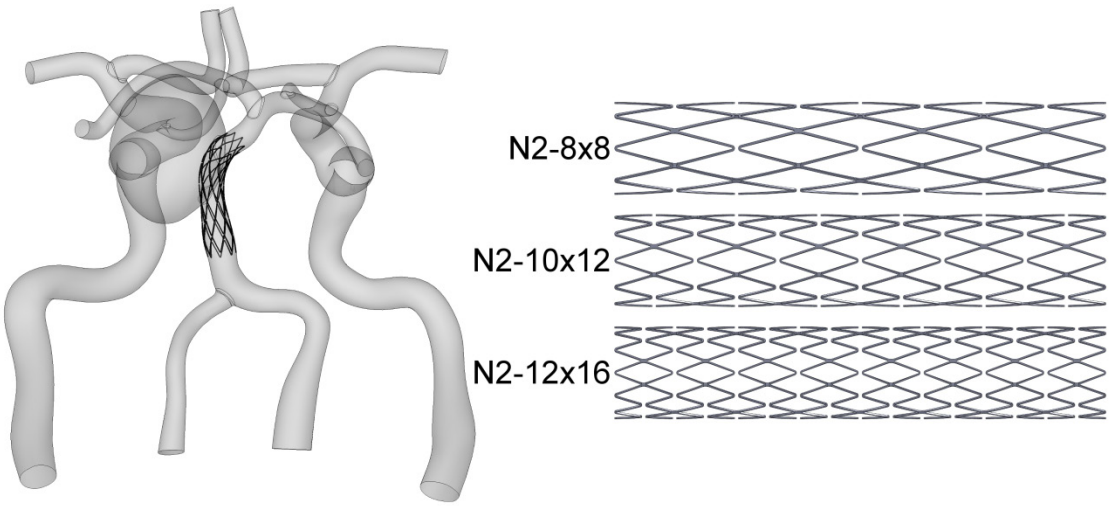

Figure 2.12: Basilar truck aneurysm in which three stents similar to the Neuroform2 were virtually implanted.

Vascular remodeling is known to occur in areas of elevated WSS. The area of the impact zone (TAWSS >20 dynes/cm^2) created by velocity impinging on the aneurysm

surface was quantified in addition to the area of low TAWSS <4 dynes/cm^2 [41, 78]. To quantify flow stasis, each model was virtually clipped at both ends of the stented region to isolate the aneurysm following simulation and convergence. MET was then computed as previously described by releasing particles at the inlet and throughout the isolated geometry.

2.5.2 Results

Three cerebral stent models and one unstented model were created using the described method of stent implantation. The stent creation and implantation into the aneurysm geometries was accomplished in about 12 hours for the N2-8x8 cerebral stent. Subsequent modification of the N2-8x8 design to create the N2-10x12 and N2-12x16 designs only took about 45 minutes per model. Using 64 cores, the final meshes of the stented (3.1 million elements) and unstented cerebral models (3.1 million elements) were simulated in 2.3 and 1.8 hours per cardiac cycle respectively.

Peak systolic velocity, TAWSS and peak systolic TKE for the three cerebral aneurysm stent designs are shown in Figure 2.13. Peak systolic velocity in the dome of the aneurysm decreased as stent filament (i.e. linkage) size decreased, as well as the size of the high velocity jets through the stent. Decreasing filament size also reduced TAWSS on the distal wall of the aneurysm, and caused the area of high TAWSS to move from the dome of the aneurysm towards the neck. The area of the impact zone (TAWSS >20 dynes/cm^2) was 7.2%, 3.2%, 2.6% and 1.7% of the total aneurysm lumen area for the unstented, N2-8x8, N2-10x12 and N2-12x16, respectively. Similarly, the area of low TAWSS (<4 dynes/cm^2) was 33.9%, 55.4%, 59.3% and 64.9%. Qualitatively, the TKE in the aneurysm was minimal throughout the cardiac cycle. Only mildly unsteady flow was

present during peak systole. Volume rendered TKE showed no apparent relationship between the TKE and stent filament size (Figure 2.13). Similarly, mean TKE values, measured in the stented region (Table 2.2) do not indicate a trend consistent with the observed decreases in velocity and TAWSS. The unstented geometry had the largest TKE, the N2-12x16 had the lowest TKE, but the N2-10x12 and N2-8x8 have similar values of TKE. The basilar artery proximal to the aneurysm had a diameter of 3.6 mm and computed peak and mean Reynolds numbers (Re) of 472 and 240 over the cardiac cycle, respectively.

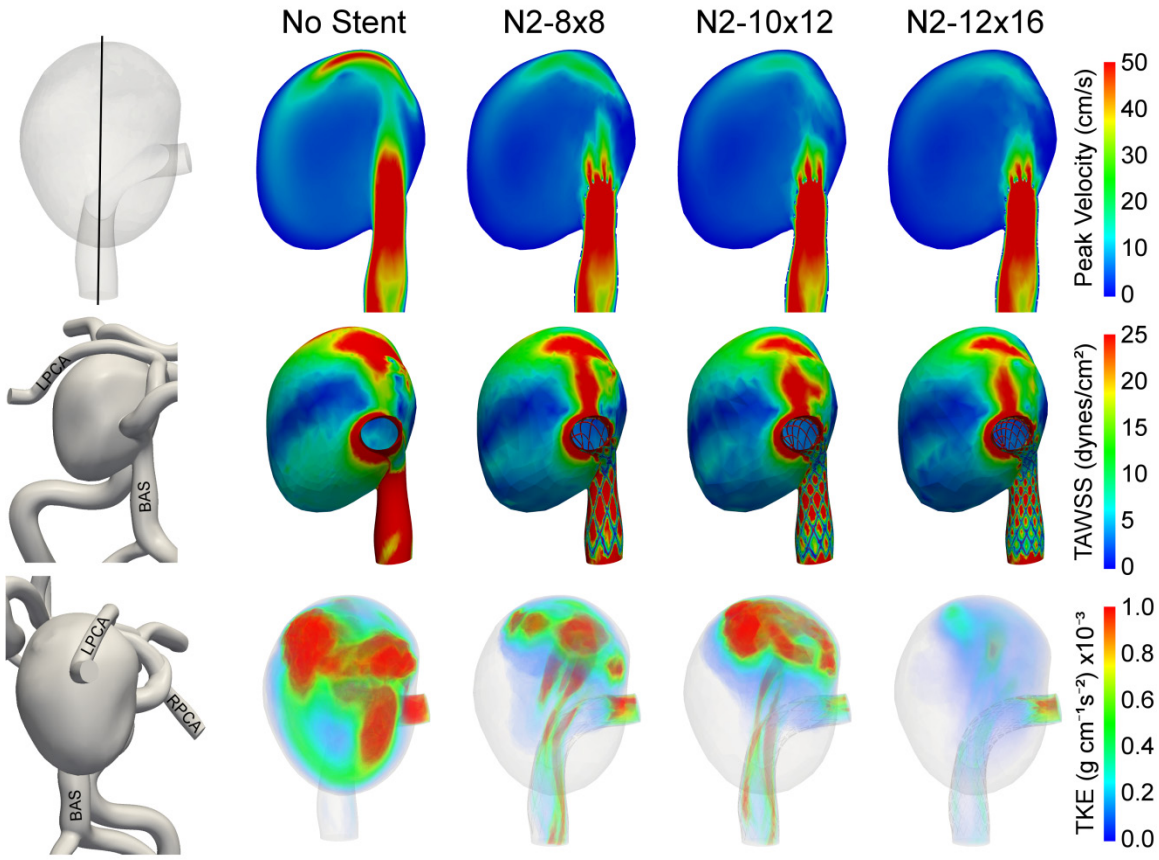

Figure 2.13: Summary of the hemodynamic indices within the stented cerebral aneurysm models. (Top) Magnitude of velocity in a slice in through the center of a cerebral aneurysm and stent during peak systole. (Middle) Time-averaged wall shear stress (TAWSS) on the lumen of the aneurysm visualized on the distal surface of the aneurysm where blood entering the aneurysm impinges on the lumen. (Bottom) Volume rendered turbulent kinetic energy (TKE) in the aneurysm at peak systole. The models on the left illustrate the position of the velocity slice and the perspectives from which TAWSS and TKE were visualized with respect to the basilar (BAS), left posterior cerebral artery (LPCA) and right posterior cerebral artery (RPCA).

Table 2.2: Mean turbulent kinetic energy (TKE) and mean kinetic energy (KE) within the cerebral aneurysm models during peak systole.

	No Stent	N2-8x8	N2-10x12	N2-12x16
TKE (g cm^{-1} s^{-2}) $x10^{-4}$	5.22	1.64	2.00	0.57
KE (g cm^{-1} s^{-2})	4.14	3.89	5.28	4.28
TKE/KE Ratio $x10^{-5}$	9.9	3.83	4.83	1.47

Mean exposure time within the unstented aneurysm model and the model stented with the N2-12x16 stent are shown in Figure 2.14. MET calculations were performed with 6.9 million particles released over the course of one cardiac cycle and tracked from

an additional 19 cardiac cycles for each model. As shown in Figure 2.14, the greatest increase in MET was near the wall of the model and in the middle of the aneurysm. The stent struts also induced a small area of high MET near the stent/lumen interface (Figure 2.14 Cross-section B of the N2-12x16). The MET field of the N2-8x8 and N2-10x12 (results not shown) exhibited similar patterns of MET to those in the unstented and N2-12x16, with magnitudes greater than the unstented and less than the N2-12x16 models. Figure 2.15 illustrates the changes in the PDF and cumulative distribution function, computed by integrating the cumulative distribution function (CDF) of the MET field within the stented and aneurysm region for the various cerebral models. With decreased stent filament size, the PDF shifted towards larger higher MET values. The CDF also indicates the unstented model has the highest volume of low MET, whereas the stented models have decreased volumes of low MET.

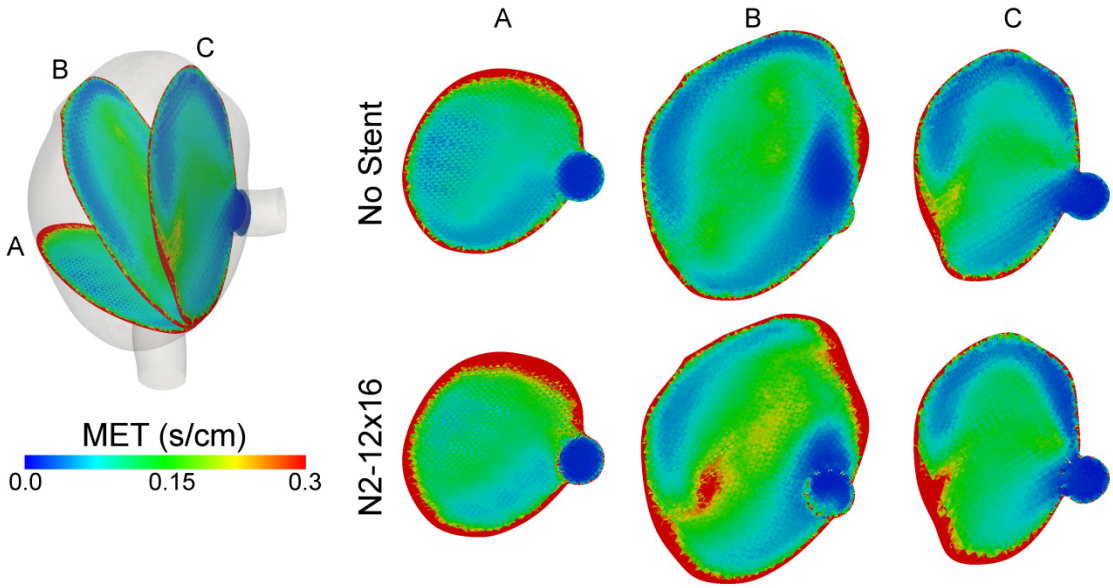

Figure 2.14: Cross-sections of the mean exposure time field at three locations within an unstented aneurysm and an aneurysm with the N2-12x16 stent across the aneurismal neck.

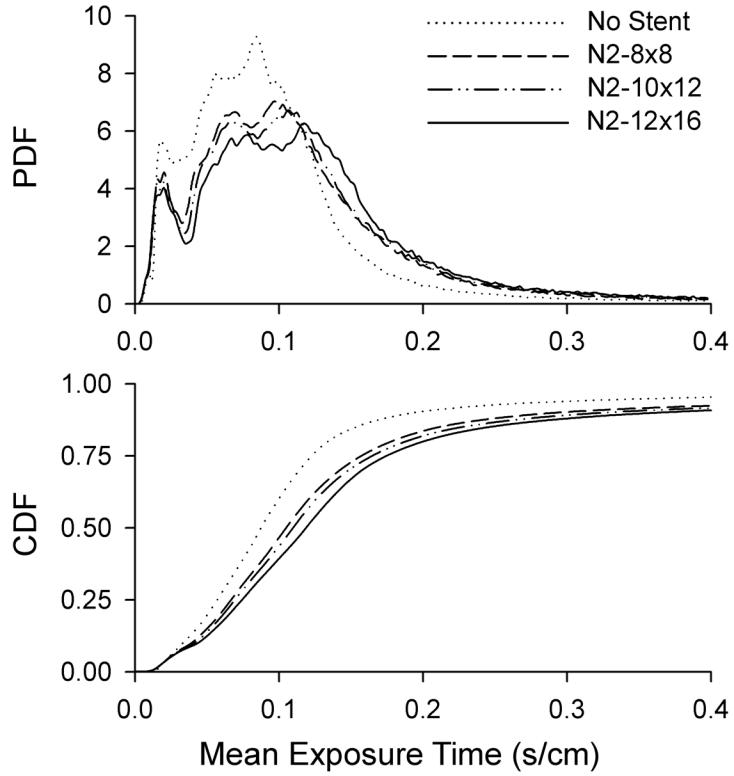

Figure 2.15: Probability density function (PDF) and corresponding cumulative distribution function (CDF) of the mean exposure time field within the aneurysm volume of four basilar trunk aneurysm models in which various stents were placed across the neck of the aneurysm.

2.5.3 Discussion

Within the cerebral aneurysm model, the velocity, MET, and WSS results indicate that stent implantation increases flow stasis, and decreased stent strut size further increases flow stasis within the aneurysm. Though the porosity of each stent was identical, velocity within the aneurysm decreased as the stent strut size decreased and reduced the area of the impact zone while increasing the area of low TAWSS. None of the stent designs completely eliminated the impact zone, so it is likely vascular remodeling would degrade the aneurysm wall in this region. Interestingly, the magnitude of TAWSS in the impact zone is similar to that in the basilar artery proximal to the

aneurysm, but the tissue response to the WSS stimuli is likely different. Recently Meng *et al.* induced basilar aneurysms in rabbits and found that diseased tissue within an aneurysm continues expanding and remodeling even after the hemodynamic stimulus that initiated aneurysm formation is removed, unlike healthy vascular tissue which ceases to remodel once stress levels return to a preferred physiologic level [77].

The results did not indicate any relationship between TKE and stent design. Overall the low Reynolds number and small TKE values in each aneurysm geometry indicates that blood flow in the aneurysm is quite steady, so it is difficult to draw any conclusion about chaotic blood flow in this region. If blood flow to this region were increased by simulating exercising conditions, differences among the stent designs may be more apparent.

The current findings coincide with those of Lieber *et al*., who showed that decreased filament size correlated with improved hemodynamic results in a previous PIV study of helical stents [68]. However, this previous study also observed pronounced stent movement with very small filament size which caused increased circulation within the aneurysm for the smallest filament size considered. By modeling the stent as rigid, stent motion was not considered in the current investigation. Another previous PIV study of twenty different stent models, including helical stents, ring-and-link stents, etc., was unable to identify a simple relationship between either stent porosity and stent performance or stent strut size and stent performance [12]. Since the present work was able to quantify the effects of strut size at a constant porosity, future work may include repeating this study with the same basic designs, but using parametric modeling techniques to model three stents with identical strut size, allowing the porosity of the

stents to vary. In this manner, it might be possible to identify which stent design parameters have the greatest influence on stent performance in cerebral aneurysms.

2.6 Discussion of patient-specific modeling techniques

2.6.1 Summary

The described virtual stenting method provides a rapid and robust means for evaluating the performance of commercially available and next-generation stents in patient-specific geometries using CFD. The complexity of the coronary bifurcation and large basilar trunk aneurysm models demonstrates the applicability of these methods across vascular beds. Though the CFD results were quantified using some custom computer programs, the model creation and stent implantation process was completed using only open source software and commercially available CAD packages already frequently used by stent design engineers. The method provides a process and examples of results that were previously difficult or laborious to obtain. Localized changes in indices known to correlate with restenosis including WSS can now be obtained for almost any conceivable stent design. Results not often reported such as intrastrut displacement due to differences in stent-induced scaffolding or parameterized contributions of design features to flow stasis can also be obtained rapidly.

Both vascular geometry and stent design are known to influence the post-procedural outcomes of stenting in most diseases treated by stenting. The method of virtual stent implantation employed in this investigation demonstrates a means of representing a complex vessel and full stent geometry to further understand the hemodynamic interactions between them. It is worth noting that other ways of virtually implanting stents into patient specific vessels have been developed previously [3, 51], but

the series of Boolean operations described here are computationally inexpensive to include and ensure the stent model is in good apposition to the vessel wall.

Using the methods outlined in this investigation, most commercially available and next-generation stents could be modeled with the exception of braided stents with a circular strut profile or other more complicated strut profiles. Stents with complex strut profiles could be generated using the same modeling techniques described in this investigation when simulating blood flow through ideal vessels, but implanting these stents in a patient-specific geometry in which the dimensions of the vessel are not well defined is not possible using the current methods. Nevertheless, the current virtual stenting process provides a framework for rapidly producing and analyzing various stent designs. In this investigation, the deployed configuration of the each stent design was modeled as using parametric design techniques enabling rapid generation of several variations for a particular stent design. Modeling the stent in a deployed configuration further decreased the amount of time necessary to numerically compute the expanded configuration of the stent. Three cerebral aneurysm stent models were all generated from the same basic design that was created and virtually implanted in the aneurysm model within a few hours after establishing the variables for use with the initial stent geometry. Given that generating, modifying, and virtual implanting a stent design using the current method can be performed quickly, this process of stent modeling is well-suited for design optimization.

In addition to presenting a novel technique of stent implantation, this investigation demonstrates post-processing techniques of CFD data which enable a better understanding of flow dynamics within stented geometries. Computation of MET

provides insight into changes in bulk flow characteristics within a volume of interest (Figure 2.14) and pinpoints specific locations of flow stasis (Figure 2.11, Figure 2.13), whereas the commonly used metric of aneurysm turnover rate only provide information about bulk flow. Moreover, aneurysm turnover is computed by quantifying the flow across a plane at the aneurysm inlet. This plane may be difficult to define within irregular patient-specific geometries, as was the case in this investigation. This investigation also demonstrates an unwrapping technique that facilitates the visualization and comparison of CFD results, such as TAWSS and displacement, within stented regions in a manner similar to that described by Antiga *et al*. [2]

2.6.2 Limitations

The current results should be interpreted within the constraints of several potential limitations. Notably, the stent implantation method does not model the mechanical interaction between the stent and the vessel during stent deployment. Accurately modeling stent deployment would require more extensive computations and knowledge of stent geometry and material along with the vessel geometry and morphology, which can be difficult to obtain *in vivo*. The described methodology does not account for compliance mismatch between the stent and vessel wall which often causes vessel straightening in curved vessels [42, 83, 115], asymmetric stent deformation across aneurysm necks or branching arteries [25, 43], kinking of the stent in regions of acute curvatures [25], vessel prolapse into the flow domain [14, 61, 85], or stent malapposition [14]. From previous CFD studies of the coronary arteries with and without straightening induced by stenting, it would be expected that extreme changes in curvature near the proximal and distal ends of stent may induce harmful distributions of WSS that leads to

restenosis [59]. Vessel prolapse has been incorporated into idealized CFD models of commercial stents and was found to decrease the amount of the vessel exposed to low WSS [85]. Conversely, previous idealized models [61] and a more recent study of stent deployment in a canine artery *ex vivo* [14] have found that prolapse of the vessel into the flow domain increased levels of WSS; therefore hemodynamic alterations due to vessel prolapse likely depends on the stent design and how prolapse is modeled. The *ex vivo* canine model of Benndorf *et al*. was also used to study stent malapposition in straight vessels and identified increased low WSS distal to the malapposition [14]. Although stent implantation method described in this investigation does not account for the stent/vessel interactions discussed above, visual comparison of the coronary model in this investigation to that of Benndorf *et al*. indicates that deviations from reality appear to be modest when this method is used in a relatively straight geometry. In vessels of acute curvature, the inability to predict changes in wall curvature and stent kinking are inherent limitations of the method described here. Future research on the virtual stent implantation methodology will work to address these limitations.

Modeling large portions of the vasculature in addition to a stent made it difficult to achieve mesh independence as defined by a change in time-averaged WSS at predetermined proximal and distal intrastrut <0.09 dynes/cm^2 between successive meshes. In the coronary stenting simulation, this level of accuracy was achieved with ~3 million elements, but was not attainable in the cerebral aneurysm models due to the computational limitations of generating large meshes for vessels over such a wide range of sizes. Therefore, conclusions regarding intrastrut distributions of TAWSS were not made for these models. Measured levels of TAWSS within a 1.5 mm thick slice of the

model proximal and distal to the stent changed by <1% for the cerebral aneurysm model. Though mesh-independence was not attained as defined, stent struts extending across the neck of the cerebral aneurysm had >5 elements across their face for simulations with the densest meshes.

2.6.3 Virtual stent implantation in retrospective models

Most of the limitations of the virtual stenting method in this investigation are only valid when creating *a priori* models using the stenting procedure. The method can also be used to reconstruct patient-specific geometries post-stent implantation with much greater accuracy since the final geometry of the deployed stent and associated vessel is known. For example, Figure 2.16 illustrates a modified version of the virtual stent implantation method using models constructed from high resolution optical coherence tomography imaging data obtain immediately following a stenting procedure [27]. In this case, the vessel lumen and outer surface of the stent were segmented and lofted separately to create two distinct models (Figure 2.16, A and D). The stent radial thickness was then subtracted from the solid model representing the outer surface of the stent (Figure 2.16, A). Subtracting the thinner lofted stent model from the thick stent yielded a patient-specific stent model that mimicked the inner surface of the stent (Figure 2.16, B and C). The final subtraction of the patient-specific stent model (Figure 2.16, C) from the lumen model (Figure 2.16, E) generated the flow domain used for subsequent CFD simulations (Figure 2.16, F). Using this modeling technique, the stent position is represented as it appears *in vivo* with the only limitation being the inability to model small non-uniform expansion of stent cells. Features such as vessel prolapse and thrombosis can also be represented in the CFD model.

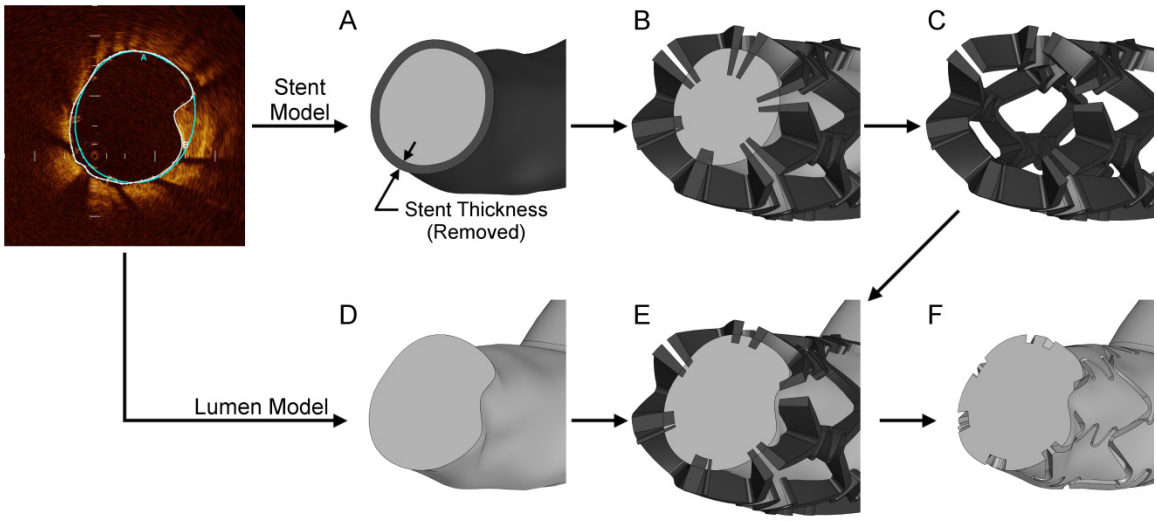

Figure 2.16: Modified virtual stent implantation method that can be used in conjunction with high resolution optical coherence tomography imaging data post-stenting procedure.

2.7 Conclusion

In summary, the current investigation describes an efficient method for virtual stent implantation in patient-specific models in order to analyze alterations in hemodynamics using CFD. Unlike idealized computational models of stent designs, this method can be used to quantify differences in stent performance in complex vascular models for most stenting procedures, as demonstrated in this investigation through the construction of two arterial models with varying degrees of complexity. For each model in this investigation, the method of virtual stent implantation was used to quantify the potential impact of partially occluding downstream vascular regions by stent struts and therefore may be used in future studies to investigate various stenting strategies at bifurcations or in response to treatments in order to provide additional insight into ways of improving stents for particular portions of the vasculature.

Chapter 3

Optimization of Cardiovascular Stent Design Using Computational Fluid Dynamics

3.1 Introduction

While previous CFD studies have provided useful insight for improving stent design, they only analyze a small number of possible stent geometries in order to identify the general trends that govern stent design. For example, computational studies of idealized stent geometries have shown that thinner struts and those more aligned with the primary flow direction decrease the amount of low WSS at the arterial wall using only three or four models [60, 62]. Similarly, within this thesis (Chapter 2, Case Study 2) only three variations of a simple flow diverting stent were modeled to investigate improved stent designs.

Conversely, incorporating a shape optimization algorithm with a proven convergence theory into the design process allows engineers to systematically identify the most favorable designs. Previous CFD optimizations of coronary stent design have been limited to 2-D stent models or optimizations of a single stent cell [6, 18, 101]. The objective of this investigation was to develop a fully automated framework for designing hemodynamically optimal coronary stents using CFD of complete, 3D stent geometries. While traditional gradient-based optimization methods often require invasive changes to

the solver code, therefore limiting potential applications, the use of a derivative-free method in this work allowed for a flexible and efficient framework. The utility of this framework is then demonstrated with two case studies of coronary stent geometries. The first case study examines the relationship between the optimal number of circumferentially repeating stent cells (N_C) and the intrastrut angle of generic slotted-tube stent design. Building on the results of the first case study, the second case study analyzes the relationship between vessel diameter and the optimal N_C for a generic slotted-tube and three commercially available stent designs. For each case study, the stent design that best maintains the homeostatic of level WSS was defined as optimal.

3.2 Methods

3.2.1 Stent and vessel model construction

Similar to the technique used for generating patient-specific stent models, stents were parameterized and modeled in an expanded state using SolidWorks. However, the previous technique for creating stent models (Figure 2.1, B1-B2) required user interaction to manually alter stent design parameters. In order for the optimization framework to be fully automated, a custom software program was written using the SolidWorks application programming interface to generate solid models of stent designs for a given set of parameters (Figure 3.1, A). The program did not generate stent models from scratch because the steps for modeling commercial stents differ slightly depending on the design, which would require a new program to be written for each design. Instead the program opened a previously parameterized stent model, altered the specified dimensions and rebuilt the model such that the same program could be used for all of the stent geometries regardless of the techniques used to create the model.

Idealized vessel models were also constructed using SolidWorks. All vessels were modeled with a stent-to-artery diameter ratio of 1.1:1 [35], but the length of the expanded stented region of the vessel differed depending on the stent design. A 2.0 mm tapered section connected the expanded stented section of the vessel to proximal and distal 5.0 mm sections of unstented vessel [86]. A Boolean subtraction operation was performed to remove the stent model from the vessel model resulting in a solid model of the flow domain (Figure 3.1, B).

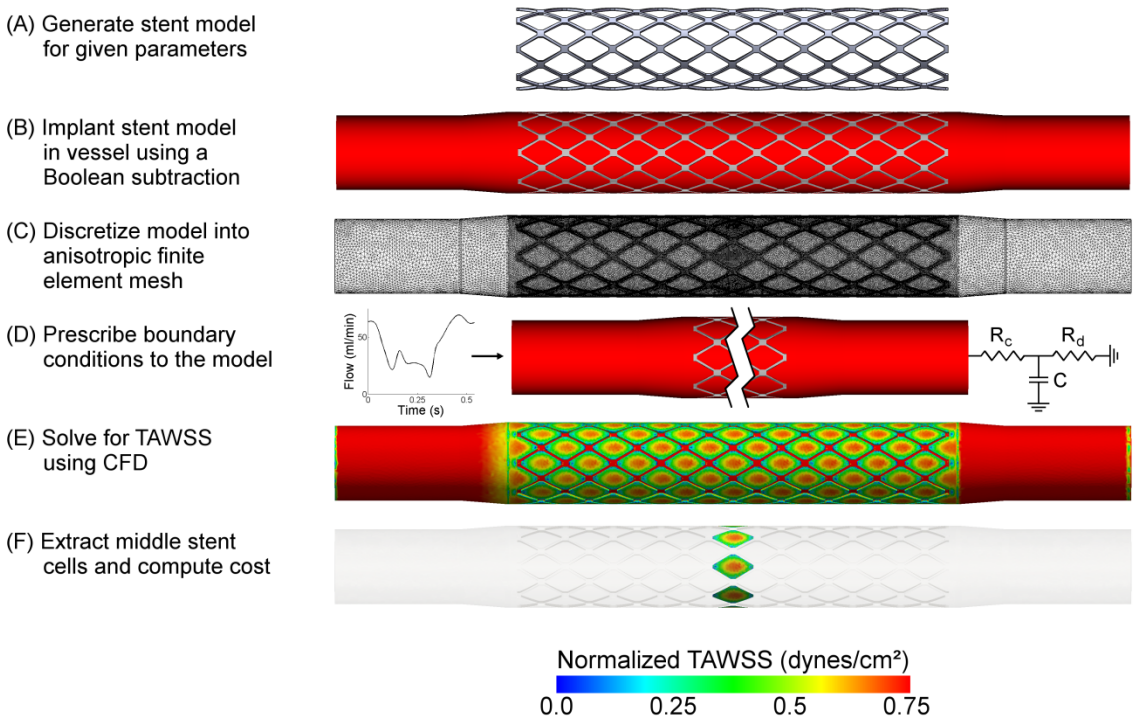

Figure 3.1: Description of the steps necessary for evaluating a stent design. The TAWSS is shown normalized to the average TAWSS in the proximal, unstented region of the model.

3.2.2 Computational fluid dynamic simulations

Solid models of the flow domain were discretized into unstructured tetrahedral finite element meshes using MeshSim. The mesh generation was tailored to create one highly anisotropic mesh for each model. A coarse mesh was prescribed in the proximal

and distal unstented regions of the vessel, with a finer mesh density prescribed to the stented region, and a very fine mesh density pres

cribed in the intrastrut regions that are later quantified as part of the optimization routine (Figure 3.1, C). Using highly anisotropic meshes ensured the near-wall hemodynamics were well resolved within the portion of the model later quantified by the optimization routine without incurring the high computational cost of dense isotropic meshes.

The boundary conditions prescribed to the discretized stent model were similar to those used for the patient-specific coronary bifurcation model (Section 2.4.1). Briefly, the artery was assumed to be rigid and a no-slip boundary condition was prescribed on the vessel and stent surfaces. Blood was assumed to be a Newtonian fluid with a density of 1.06 g/cm^3 and a viscosity of 4 cP. A time-varying canine left-anterior descending coronary artery flow waveform [57] with characteristics similar to those found in humans was imposed at the model inlet using a Womersly velocity profile (Figure 3.1, D). The inflow rate was not scaled for different diameter vessels. Outlet boundary conditions were prescribed using a three-element Windkessel approximation to replicate the physiologic impedance of the downstream vasculature (Figure 3.1, D). The outlet boundary conditions were modified to account for the resistance of ventricular contraction as previously described (Section 2.4.1).

CFD simulations were run using an in-house stabilized finite element solver with commercial linear solver component LESLIB (Altair Engineering, Troy, MI) to solve the time-dependent Navier-Stokes equations. The time-step was chosen for a Courant, Friedrichs and Lewy condition <1. Simulations were run until the outlet pressure and

flow were periodic, defined as a maximum error between equivalent points in successive cardiac cycles <1 mmHg and <1mm^3/s. TAWSS was then computed over the last cardiac cycle as previously described (Section 2.3.1). Cells in the middle of the stented region were extracted for subsequent evaluation in the optimization routine (Figure 3.1, F).

3.2.3 Computing design cost

The formulation of the optimization cost function was based on the physiologic theory of TAWSS homeostasis, which suggests vessels remodel to maintain a nominal level of TAWSS. Favorable stent models were defined as those which would theoretically attenuate vascular remodeling within the stented region by minimizing the disparity between TAWSS in the stented region of the model ($\overline{TAWSS}_{IS}$) and the nominal level of TAWSS in the unstented region of the model ($\overline{TAWSS}_{US}$). Thus the design cost (J) of a stent model was expressed using a ratio of $\overline{TAWSS}_{IS}$ to $\overline{TAWSS}_{US}$ as:

$$J = 1 - \frac{\overline{TAWSS}_{IS}}{\overline{TAWSS}_{US}}$$

in which $\overline{TAWSS}_{IS}$ is defined as the integration of TAWSS over the intrastrut surfaces (s) normalized to the area of those surfaces:

$$\overline{TAWSS}_{IS} = \frac{\int_s TAWSS\, ds}{\int_s ds}$$

The value of $\overline{TAWSS}_{IS}$ was computed over the intrastrut regions with the highest mesh resolution (Figure 3.1, C). This computation also mitigated any effects of slightly varying stent lengths and flow disruptions near the ends of the stented regions. A custom software program that used the Visualization Toolkit (VTK, Kitware, Clifton Park, NY) libraries

was written to compute the integral described above. The nominal level of TAWSS in the unstented portion of the vessel was computed as:

$$\overline{TAWSS}_{US} = \frac{4\mu Q}{\pi r^3}$$

where Q is the mean flow, μ is the viscosity and r is the vessel radius.

3.2.4 Optimization routine

The surrogate management framework (SMF) previously described by Booker *et al.* and applied to cardiovascular engineering problems by Marsden *et al.* was used to determine optimal stent designs [19, 73]. The general formulation of the optimization is given by:

$$\text{minimize } J(\boldsymbol{x})$$

$$\text{subject to } \boldsymbol{x} \in \Omega$$

where J represents the cost function for a given vector of parameters x in the domain Ω. The SMF framework is a derivative-free optimization algorithm that relies on pattern search theory for convergence of the cost function to a local minimum. The method restricts all parameters to lie on a discrete parameter mesh that may be refined to increase the resolution of the parameter space as the algorithm progresses. The implementation of the SMF algorithm in this investigation used a mesh adaptive direct search (MADS) polling method, which has a stronger convergence theory compared to previous generalized pattern search methods [7]. Used by itself, the MADS pattern search method may require numerous cost function evaluations to converge on a local minimum, which would be detrimental to this investigation since computing the cost of a single stent design is computationally expensive (requires model generation, meshing and time-

dependent CFD). The SMF uses a surrogate function to approximate the "true cost function" and predict the location of the local minimum, thereby increasing the efficiency of the optimization by reducing the number of cost function computations necessary to search for the location of the minimum [19]. Though various surrogate functions can be used with the SMF method, this investigation incorporated a Kriging surrogate function using the MATLAB DACE package [72] to easily extend this approach to multiple dimensions and avoid problems of overshoot found in polynomial interpolation.

The SMF optimization algorithm is schematically illustrated in Figure 3.2. The algorithm is initialized using Latin Hypercube Sampling (LHS) to generate a well-distributed set of input variables, or trial points, over the discrete parameters space [75]. Stent models are constructed and evaluated for each trial point and the resulting cost function values are used to construct the initial surrogate function.

The optimization loop consists of two fundamental steps, SEARCH and POLL. During the SEARCH step, the surrogate function is used to predict the location of parameters that minimize the cost function. If evaluation of the trial points generated by the SEARCH steps improves the current best point, another SEARCH steps ensues. After every SEARCH step, the surrogate function is updated to incorporate all new cost function values. If the SEARCH step fails to improve the current best point, a POLL step is performed. MADS is used to identify a set of n+1 positively spanning POLL points that neighbor the current minimizing point, where n is the number of parameters [7]. If the POLL step succeeds in improving the current best point, the algorithm returns to the SEARCH step. If the POLL step is not successful, then a mesh local optimizer has been found, and the optimization algorithm will either complete, or the parameter mesh will be

refined. In this investigation, refining the parameter space decreased the parameter mesh size (Δ_m) by ¼. When the POLL step fails and the parameter mesh has been refined to the specified tolerance, the optimization algorithm stops.

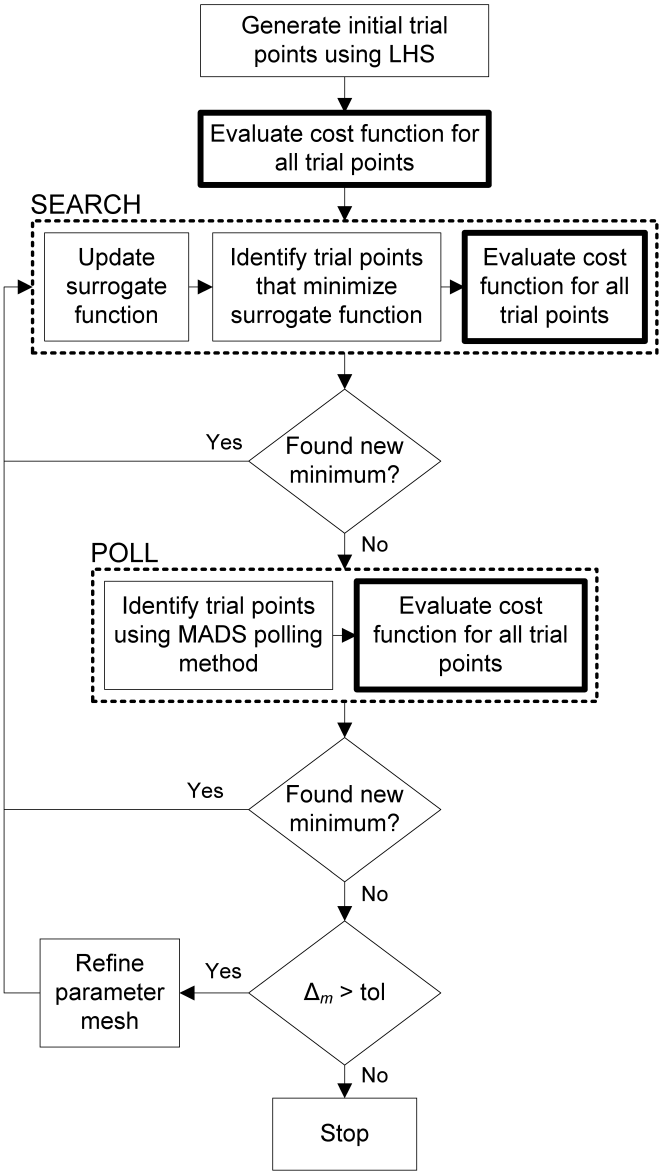

Figure 3.2: Flowchart of the Surrogate Management Framework optimization routine. Each bolded box indicates a point in the routine where the cost function for a stent design is evaluated. The optimization stops when the size of the discrete parameter mesh (Δ_m) is refined beyond a user specified tolerance (tol).

To fully-automate the optimization routine, the optimization algorithm was coupled to the cost function evaluation using TCL scripting capabilities within

Simvascular (www.simtk.org). The scripts called external programs to execute the optimization algorithm (MATLAB), build models (SolidWorks), perform CFD, and compute cost values (VTK). Because MeshSim is directly integrated into Simvascular, meshing and prescribing boundary conditions was performed using built-in Simvascular subroutines. The majority of the optimization routine was executed on a standard personal computer except for the CFD simulations, which were performed on a high performance computing cluster.

During some steps of the optimization routine the parameters of multiple trial points may be known, such as during the LHS and POLL steps, in which case the cost of multiple stent models can be computed simultaneously for increased efficiency. The initial implementation of the optimization framework serially evaluated the cost of multiple trial points whereby each stent model was built (model construction and meshing), run (CFD) and quantified (compute cost) before another model could be evaluated. It was later determined that TCL's multithreading abilities could be used to evaluate trial points in parallel by spawning a new thread to build, run, and quantify each model. Using this approach, evaluating multiple models would theoretically take the same amount of time as evaluating a single model. Unfortunately, in this investigation it was not possible to build several models in parallel due to the memory constraints of the desktop computer used. Nevertheless, the CFD simulations could still be run in parallel, since this portion of the optimization was performed on a computer cluster in which there were no memory constraints. Thus trial points were evaluated in a pseudo parallel fashion in which each model was serially built, but a new thread was spawned to run and quantify the model. This approach still provided better performance than serially evaluating

multiple trial points, but the efficiency of the optimization could be further improved by evaluating multiple trial points in parallel in future studies, possibly by transferring the modeling building code to high performance computing cluster. The difference between serial, pseudo-parallel and parallel is illustrated in Figure 3.3.

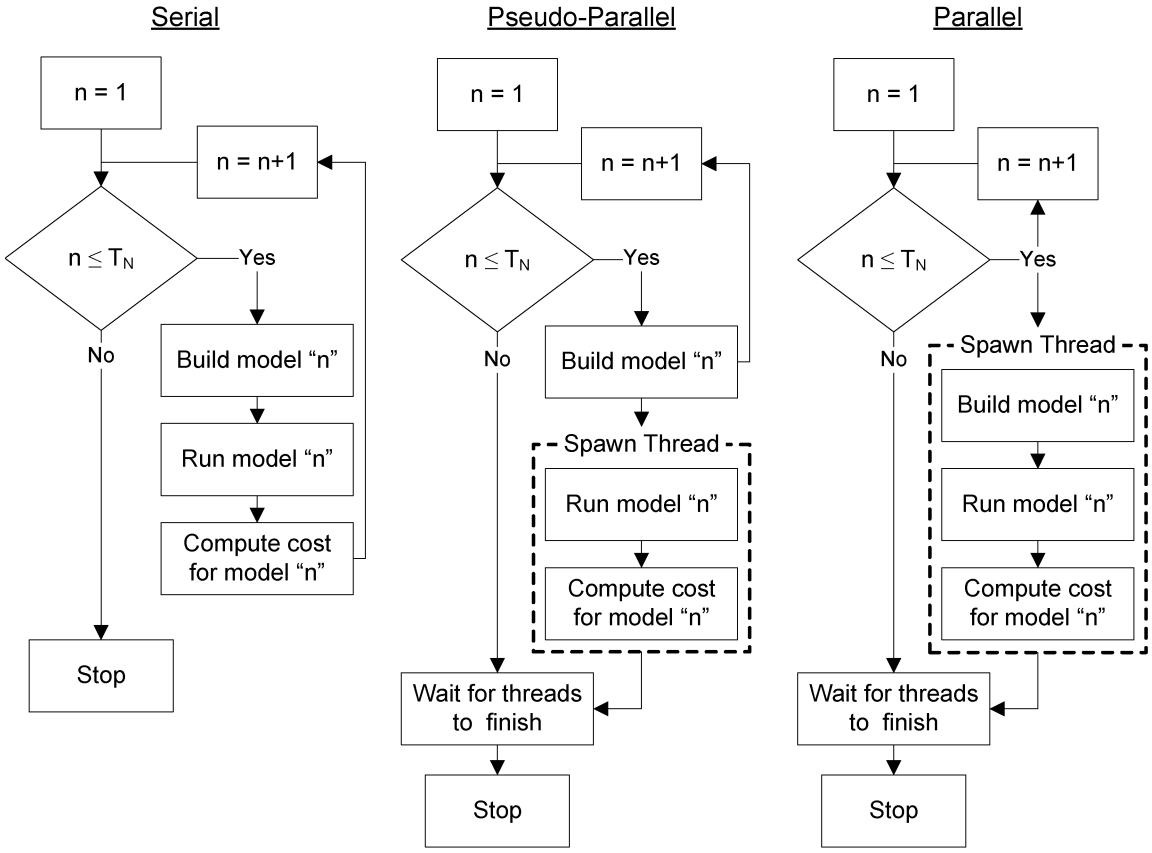

Figure 3.3: Comparison of serial, pseudo-parallel and parallel algorithms of evaluating multiple trial point during the optimization a stent design. Each algorithm is illustrated with a flow chart of the various steps necessary to evaluate the total number (T_N) of stent models. Note that the parallel and pseudo-parallel algorithms spawn new threads to simultaneously execute certain portions of the algorithm and increase the performance of the optimization.

3.3 Case Study 1: Optimization of a generic slotted-tube stent with a constrained intrastrut area

A previous CFD study of slotted-tube stent designs indicated stents which minimize the number of stent strut intersections reduce the area of the vessel exposed to

potentially deleterious levels of low TAWSS [60]. Because this study only compared two stent designs and varied both N_C along the number of axial repeating stent cells (N_A), it is difficult to isolate the hemodynamic effects of either N_C or N_A. To further understand the effects of these parameters, this case study aimed to simply optimize N_C. During the course of this investigation, it was hypothesized that the strut angle relative to the primary direction of flow may dictate the optimal value of N_C. Therefore, a second set of optimizations was performed to determine if the optimal strut angle correlates with the optimal values of N_C computed in the first optimization.

3.3.1 Parameterization of stent models

Generic slotted-tube stents, similar to the Palmaz-Schatz design, were generated from a parameterized stent model in which the cell axial length (l_a), circumferential distance between adjacent struts (l_c) and intrastrut angle (θ) could be altered (Figure 3.4). Stent strut radial thickness and intrastrut area were explicitly defined to prevent the optimization routine from pursuing infeasible stent designs since the objective of maintaining the homeostatic level of TAWSS within a stented vessel is ideally met by a stent design with negligible strut thickness and large intrastrut areas if these parameters are not kept constant. This intuition was confirmed by preliminary optimizations before the strut width and thickness were defined as 100μm, similar to the size of an average stent. The intrastrut area of commercial closed-cell stents varies between 1mm^2 and 3mm^2, and an ideal area is not known. Therefore optimizations were performed with intrastrut areas of 1mm^2, 2mm^2 and 3mm^2 (Figure 3.4) to examine the effect of this parameter on optimal stent design within the range of commercial stent designs.

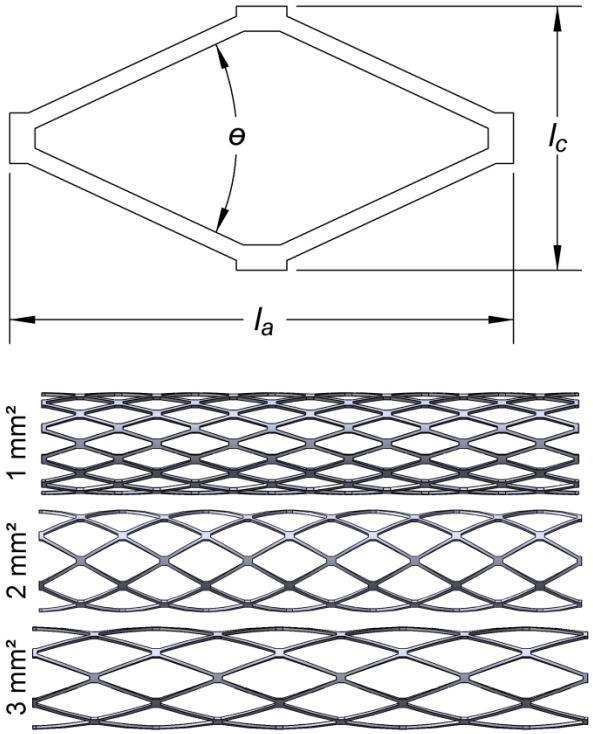

Figure 3.4: (Top) Parameterized drawing of a stent cell which is characterized by the cell axial length (l_a), circumferential distance between struts (l_c) and intrastrut angle (θ). (Bottom) Examples of three stent models with different intrastrut areas shown to the left of each model.

Vessels were modeled with an expanded, or stented, length of 18 mm. With the addition of an unstented and a tapered section, the total model length was 32 mm. To analyze the effect of vessel diameter on optimal stent designs, all optimizations were performed in both small (SV) and large vessels (LV) with diameters of 2.25 mm and 3.0 mm corresponding to stent diameters of 2.475 mm and 3.3 mm, respectively.

3.3.2 Method for optimizing the number of circumferentially repeating stent cells

When determining the optimal value of N_C for a given stent design the intrastrut area and vessel diameter remained constant while N_C was allowed to vary. To determine the cell geometry for a given N_C, l_c was computed based on the stent diameter and the value of N_C specified by the optimization routine. The axial cell length was then

computed to maintain a constant intrastrut area of either 1mm^2, 2mm^2 or 3mm^2. Lastly, N_A was computed to achieve a target stent length of 18mm or less.

The optimal value of N_C was computed for each combination of vessel size and intrastrut area for a total of six stent design optimizations. For each optimization, the initial parameter mesh was defined to include all possible integer values. The parameter mesh was not refined during the optimization since N_C was not a continuous variable.

3.3.3 Method for optimizing the intrastrut angle

The model construction method described in the previous section could not be used to optimize θ because the constraints of an integer number of circumferentially repeating cells and a constant intrastrut area only allows for the creation of stent models with discrete θ values. Instead, stent models were created in which θ was a continuous variable and consequently, N_C was also allowed to be a continuous variable. Models created using this approach had a repeating strut configuration that propagated around the circumference of the vessel, but did not necessarily meet to form a continuous pattern (Figure 3.5). While this approach may not create feasible stent designs, it does provide a means of investigating the optimal intrastrut angle with fine detail. To create a stent model for a given θ, l_a was first computed to maintain a constant intrastrut area of either 1mm^2, 2mm^2 or 3mm^2 and subsequently N_A was computed to achieve a target stent length of 18 mm.

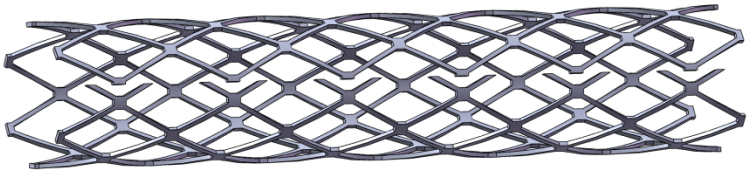

Figure 3.5: An example of a stent model that was generated when optimizing the intrastrut angle. Note that the number of circumferentially repeating cells was not constrained to being an integer resulting in an infeasible stent model that appears broken.

As with the optimization of the number of repeating circumferential units, the optimal θ was computed for each combination of vessel size and intrastrut area. The intrastrut angle was a continuous variable so initial parameter meshes were defined as have a spacing of 8° with three refinements performed during the optimization. This resulted in a final parameter mesh resolution of 0.5°.

3.3.4 Results of optimization of the number of circumferentially repeating stent cells

The number of circumferential repeating cells was optimized for stent designs with intrastrut areas of 1mm^2, 2mm^2 and 3mm^2 in both large and small vessel models. The optimal design parameters are summarized in Table 3.1. For stent designs with equivalent intrastrut areas, the optimal number of circumferential repeating cells increased with increased vessel size, and the optimal cost was lower in the small diameter vessel (e.g. SV-1mm^2: N_C=7, J=0.590 vs. LV-1mm^2: N_C=9, J=0.613). Within vessels of the same diameter, the optimal cost decreased with increased intrastrut area (e.g. SV-1mm^2: J=0.590 vs. SV-2mm^2: J=0.500). Each optimization converged on an optimal design using seven or fewer function evaluations.

Table 3.1: Results from optimizing the number of circumferentially repeating stent cells.

Stent Design	Cost (J)	Circumferential Repetitions (N_C)	Number of Function Evaluations
SV (Ø = 2.25 mm)			
1mm^2	0.590	7	6
2mm^2	0.500	5	6
3mm^2	0.460	4	4
LV (Ø = 3.0 mm)			
1mm^2	0.613	9	7
2mm^2	0.520	7	5
3mm^2	0.477	6	5

SV=small vessel; LV=large vessel

Plots of the cost function versus the number of circumferentially repeating cells and corresponding intrastrut angles are shown in Figure 3.6. Visual inspection of intrastrut TAWSS distributions (Figure 3.6) indicates that designs with less than the optimal number of repeating circumferential units exhibited a greater area of low TAWSS as a result of struts that were more misaligned with the primary direction of flow and decreased cell axial length. Stent designs with greater than the optimal number of circumferentially repeating cells also exhibited a greater area of low TAWSS. In this case the increased area of low TAWSS resulted from the close proximity of adjacent struts which decreased near wall blood flow velocity, and subsequently TAWSS, within the intrastrut region.

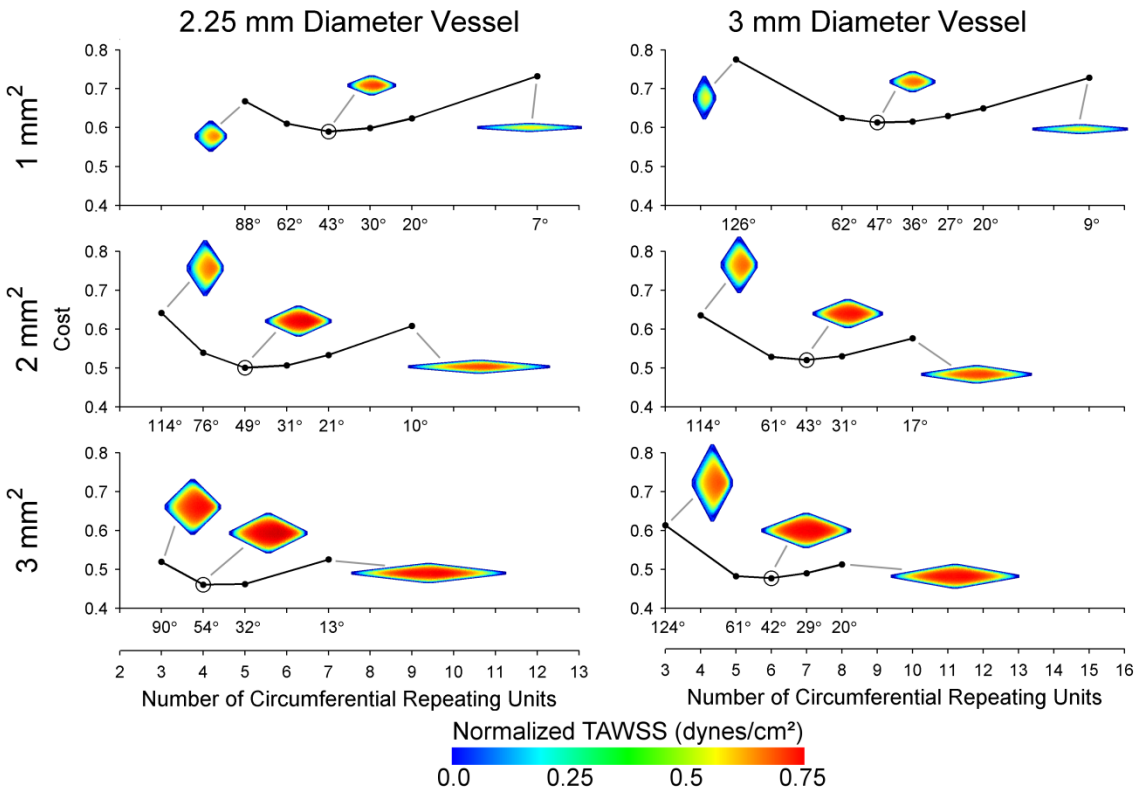

Figure 3.6: The cost function versus the number of repeating circumferential units for stent models with various intrastrut areas in a small vessel (left) and large vessel (right). The intrastrut angle corresponding to the number of repeating units is denoted on the individual plot axes for each design and the optimal design is circled on each plot. Patterns of normalized $TAWSS_{IS}$ are shown for the least, most and optimal number of circumferential repeating units.

3.3.5 Results of optimization of intrastrut angle

When the intrastrut angle was allowed to vary continuously, the optimal θ was found to be between 38.5° and 46.5° for all stent designs. This indicates that the optimal intrastrut angle is largely independent of the vessel size and intrastrut area. Plots of the design cost relative to the intrastrut angle are shown in Figure 3.7 (black lines). For comparison, the cost from the optimization of the number of circumferentially repeating cells is also shown in Figure 3.7 (gray lines). The optimal number of circumferentially repeating cells (Figure 3.7. gray circles) corresponds to the stent design closest to the

optimal intrastrut angle, indicating that the intrastrut angle dictates the optimal number of circumferentially repeating units.

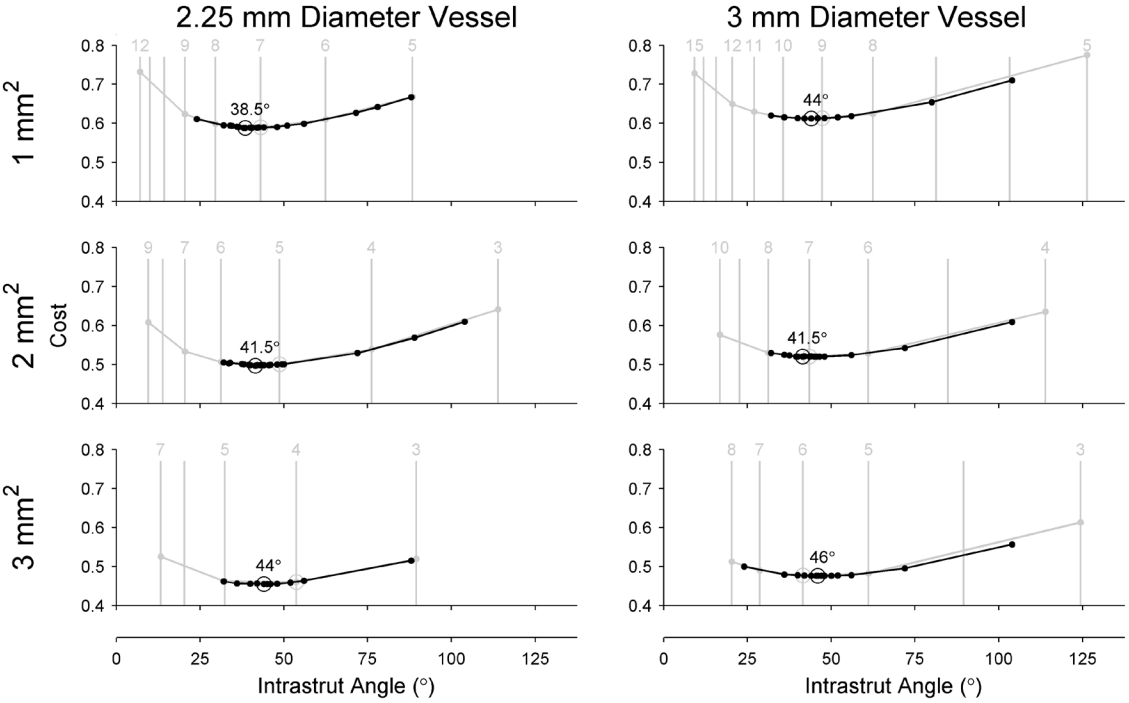

Figure 3.7: The cost function versus the intrastrut angle for stent models with various intrastrut areas in a small vessel and large vessel (black). The intrastrut angles that correspond to feasible stent designs are shown as vertical lines (gray). The cost function versus the number of circumferentially repeating stent cells is plotted along gray lines and the number of circumferentially repeating cells is denoted above the lines for models that have been evaluated. Optimal stent designs are circled on all plots.

The convergence history for the optimization of intrastrut angle is shown in Figure 3.8. LHS accounted for the first three function evaluations. Although the optimization method allowed for three mesh refinements, all optimization runs converged with less than 20 function evaluations, with the majority of runs only requiring 10 to 15 function evaluations.

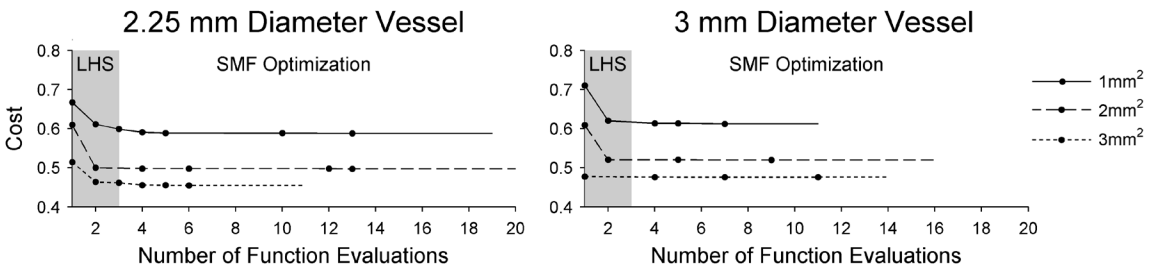

Figure 3.8: Convergence history for the optimization of intrastrut angle for stent models with various intrastrut areas in a small vessel and large vessel. The Latin Hypercube Sampling (LHS) portion of the optimization routine is shaded in gray. The Surrogate Management Framework (SMF) represents the portion of the optimization algorithm that used alternating SEARCH and POLL steps to converge on the optimal stent design.

3.3.6 Discussion

The application of the optimization produced two novel findings pertaining to the optimal design of a generic slotted-tube stent. The optimal number of circumferential repeating stent cells is dependent on the intrastrut angle, and the optimal intrastrut angle is independent of both vessel size and the intrastrut area of the stent cell. It should also be noted that the inflow waveform to the models was kept constant for both vessel diameters in this investigation, which created a large difference in the magnitude of TAWSS between the different diameter vessels as a result of the cubic relationship between TAWSS and vessel diameter. Thus, it can also be concluded that the optimal intrastrut angle is independent of the magnitude of TAWSS.

The current results confirm and extend the findings of previous stent CFD studies. In a previous study of stent foreshortening, stents with intrastrut angles of 58°, 68° and 78° degrees were constructed, and it was determined that stents with struts more aligned with the primary direction of flow decrease the area of low WSS [62]. Because angles less than 58° were not tested, this study was unable to determine that further decreasing the intrastrut angle (<40°) would actually increase the area of low WSS, as was shown in

this investigation. Numerous 2D and 3D studies have also found that increasing the axial distance between struts, effectively increasing the intrastrut area, is hemodynamically advantageous, as it allows for a greater area of flow reattachment between the struts [16, 40, 60]. In the current results this trend was also demonstrated among stent designs in vessels with the same diameter. For these models, the cost function decreased for designs with a greater intrastrut area, indicating a greater intrastrut area is hemodynamically advantageous.

To prevent the optimization from converging on an infeasible design solution in which there is no flow obstruction (i.e. no stent) in the vessel, stent thickness and intrastrut area were kept constant in this investigation. Intuitively, decreasing stent thickness and increasing intrastrut area would increase TAWSS, but this may reduce the radial strength of the stent and subsequently inhibit the ability of a stent to maintain arterial patency. Because of the mechanical constraints of stent design, the optimal strut thickness and intrastrut area cannot be determined based solely on stent hemodynamics.

3.4 Case Study 2: Identification of optimal coronary stent designs based on vessel caliber

Target vessel caliber is a known predictor of restenosis following percutaneous stent implantation for the treatment of coronary artery disease [26, 42]. Rates of restenosis are significantly higher in patients with small diameter vessels since even a small amount of neointimal growth can severely restrict blood flow and require revascularization. Even when DES are used to inhibit neointimal growth, rates of restenosis remain high in this difficult patient subset [21, 49]. Depending on the definition applied, treatment of small vessel lesions constitutes 35-67% of percutaneous

interventions [81]. In contrast, large coronary vessels can sustain a greater amount of neointimal growth before requiring revascularization, and the use of DES over BMS in vessels >3.5 mm in diameter may not even be necessary [104].

Currently stent designs are often altered based on the vessel diameter in which the stent is deployed. While the underlying pattern of the stent design is not changed, the number of circumferentially repeating crowns or crests (N_C) is increased for vessels of a larger caliber and vice versa. For larger vessels, the increase in N_C provides more scaffolding and allows the stent to be expanded to a greater diameter. As demonstrated by the previous case study, increasing N_C with increasing vessel diameter may also be hemodynamically advantageous.

Building on the work of the previous case study (Section 3.3), the objective of the current investigation was to further analyze how vessel diameter affects the hemodynamically optimal stent configuration for both a generic slotted-tube stent along with three commercially available stents. In contrast to the previous case study, this investigation reframes the optimization problem in a manner that enables the relationship between vessel diameter and the optimal stent design stent to be examined in more detail than using discrete vessel diameters. Previously the vessel diameter and intrastrut area were kept constant and the optimal stent configuration was computed for vessel diameters of 2.25 mm and 3.0 mm. In this investigation, the stent configuration is kept constant and the optimal vessel diameter is computed. With this approach the expanded stent geometry is approximated for any diameter vessel in a manner that mimics the realistic expansion of a stent. Interestingly, this reframing of the optimization problem causes both the intrastrut area and intrastrut angle to vary for vessels of differing diameters. As a stent

expands the angle of the struts becomes more misaligned with the primary direction of flow resulting in localized areas of low WSS adjacent to misaligned struts. This suggests increasing N_C may be hemodynamically advantageous as it would reduce the degree of strut misalignment. In contrast, reducing N_C generally increases the intrastrut area of the expanded stent, allowing for a greater area of flow reattachment and higher WSS between stent struts. It is therefore hypothesized that there exists a hemodynamically optimal stent configuration in which the competing effects of strut misalignment and increasing intrastrut area are balanced.

3.4.1 Stent and vessel model construction

The designs of a generic slotted-tube stent (Figure 3.9, Stent A) along with three designs that resemble commercially available stents (Figure 3.9, Stents B-D) were investigated. Stents B and C were based on the BX Velocity (Cordis, Bridgewater, NJ) and Express^2 (Boston Scientific, Natick, MA) stents respectively. Stent D was not based on any single stent design, but rather represents a simplified version of the Multi-Link family of stents (Abbott Vascular, Redwood City, CA), which includes the Vision, Mini Vision, Ultra and Zeta. The chosen stents geometries correspond to peak-to-peak (A and B), peak-to-valley (D), and hybrid (C) designs.

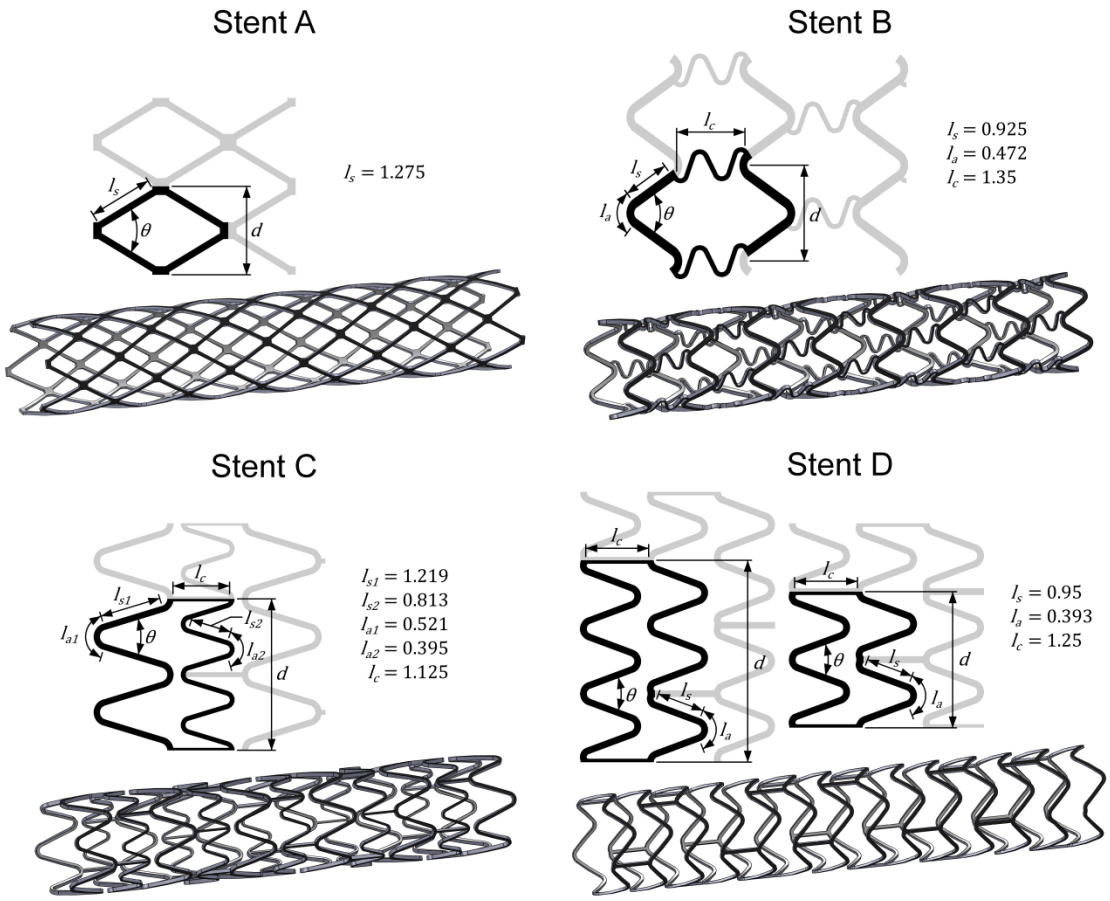

Figure 3.9: The geometry of a single cell with related dimensions along with an expanded configuration for each of the stent designs. All of the dimensions of the stent cells are given in millimeters. Each of the expanded stents shown has a diameter of 3.3 mm. Stents A, B, and C are shown with a six crown configuration whereas stent D is shown with five crown configuration that incorporates both the two and three crown cell geometries.

The geometry of a single cell of each design is illustrated in Figure 3.9 along with the dimensions relevant for approximating the expanded geometry of the stent, including the strut length (l_s), arc length (l_a) and connector length (l_c). The dimensions of stents B, C and D were based on product literature distributed by the manufactures. When generating a stent model, parameter d was computed based on vessel diameter and N_C. Although the intrastrut angle (θ) is shown in Figure 3.9, it was not used to define the cell geometry. Rather the intrastrut angle was used extensively to quantify the results of the

optimizations as it provides a design independent measurement of the expanded stent geometry. The strut radial thickness and width for each design is given in Table 3.2. All stents were modeled using the 18 mm version of the stent, with the exception of Stent C which was modeled as 16 mm since an 18 mm Express^2 stent is not available.

Table 3.2: Strut dimensions for each of the stent designs in Figure 3.9.

	Macro Struts		Micro (or link) Struts	
Stent Design	Radial Thickness (μm)	Width (μm)	Radial Thickness (μm)	Width (μm)
A	100	100	—	—
B	140	143	140	60
C	132	91	132	61
D	81	100	—	—

In the case of stents A, B and C, the number of circumferential repeating cells was simply varied to generate models with different values of N_C. It should be noted that N_C refers to the number of circumferentially repeating crowns, not the number of repeating cells (e.g. Stent C, N_C=6 corresponds to 3 circumferentially repeating cells). Because the commercial versions of stent D contain both two and three crown cell geometries, permutations of stent D were allowed to incorporate both cell geometries into a single model. To distinguish between the various permutations, designs of stent D are referred to by the number of crowns and the cells used to create the design. For example, 6-3:3 and 6-2:2:2 both refer to six crown designs but constructed with different permutations of cells.

During the optimization of a single stent design, the stent configuration (i.e. N_C) was kept constant and the expanded geometry of the stent was modeled for the vessel diameters chosen by the optimization routine. The expanded geometry was approximated by constraining the strut and arc lengths to be constant. This enabled quick generation of

stent models using SolidWorks. For stent design B, which incorporated a flexible link, it was assumed that the link maintained its shape across all diameters.

Since the vessel diameter was allowed to vary during the optimization routine, a separate vessel model was generated for each stent model. The solid model of each vessel was constructed after the stent model was generated such that the expanded portion of the vessel could be modeled to the exact length of the expanded stent. In this manner the effects of stent foreshortening would also be incorporated in to the model (Figure 3.10).

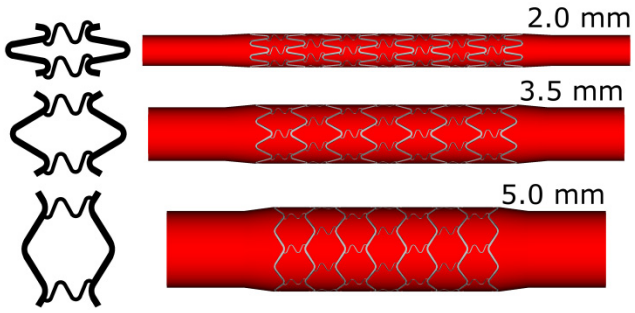

Figure 3.10: Illustrations of the expanded geometry of single stent cell (left) that was used to generate the three representative solids models of an idealized stented coronary (right). The vessel diameter depicted above each model corresponds to stent diameters of 2.2 mm, 3.85 mm and 5.5 mm. The six crown configuration of Stent B is depicted in each model.

3.4.2 Computational simulation and optimization methods

In the previous case study of slotted-tube stents, the greatest CFD mesh density was simply assigned to the stent cells in the middle of the stented region of the model. The middle stent cells were more difficult to define for the more elaborate designs of the commercial stents. For this case study, the middle stent cells were consistently determined by placing a plane through the middle of the vessel perpendicular to the direction of blood flow. Then the greatest mesh density was assigned only to intrastrut cells that intersected this plane (Figure 3.11). These cells also represent the surface over

which $\overline{TAWSS}_{IS}$ was computed. Depending on the stent model and vessel diameter, this meshing technique resulted in mesh sizes between 2.5 and 7 million elements.

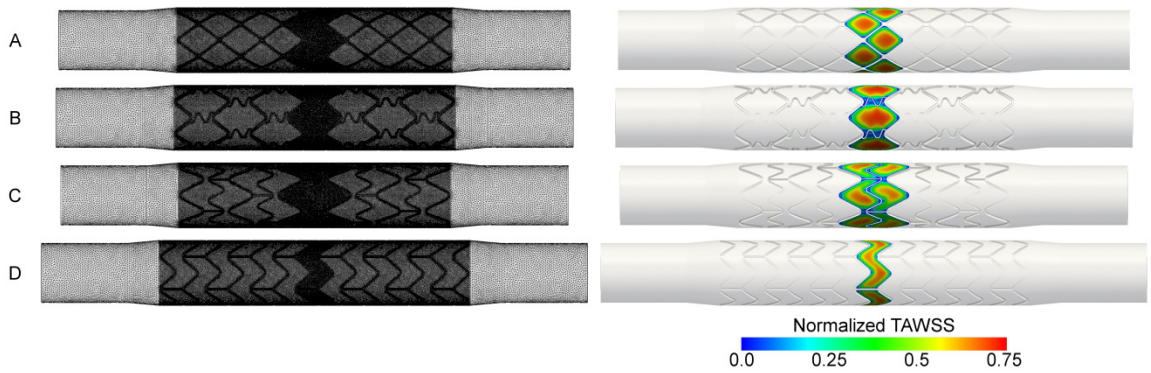

Figure 3.11: (Left) Anisotropic CFD meshes for stent designs A, B, C and D. (Right) TAWSS depicts on the stent cells are extracted and quantified during the optimization routine. TAWSS is shown normalized to the analytically computed value of TAWSS in an unstented portion of the vessel.

To determine the optimal vessel diameter for a given stent configuration, a one-dimensional parameter mesh was constructed for a range of vessel diameters between 2.0 and 5.0 mm with an initial spacing of 0.5 mm. Over the course of the optimization, the parameter mesh was refined three times resulting in a final parameter mesh resolution of 0.03125 mm.

3.4.3 Results

Some optimizations converged to the boundary of the allowable vessel diameter range (Table 3.3). Only 6-7 function evaluations were necessary in these cases, corresponding to the three vessel diameters of the initial set of design points and the three mesh refinements necessary to provide convergence to the boundary. In cases where the optimization did not converge to a boundary of the allowable vessel diameter range, the optimization routine required 9-18 function evaluations regardless of stent design. Each

optimization required four to seven days to complete depending on the number of function evaluations required.

The optimal vessel diameter was identified for four stent designs in various configurations (i.e. different values of N_C) for a total of 21 optimizations. The results of each optimization are summarized in Table 3.3. As expected, the hemodynamically optimal vessel diameter increased as N_C increased for all stent designs (e.g. A N_C =6, Ø=2.63 mm vs N_C=7, Ø=3.13 mm). For designs A, B and C, the cost of the optimal design also increased with increasing vessel diameter (e.g. A N_C=6, J=0.526 vs N_C=7, J=0.535). This trend is less apparent for stent D, in which the optimal cost did not increase between the 4-2:2 and 5-2:3 designs or 6-2:2:2 and 7-2:2:3 designs.

Table 3.3: Optimal design cost and model parameters for each stent configuration.

Circumferential Repetitions (N_C)	Cost	Vessel Diameter (mm)	Intrastrut Angle (°)	Number of Function Evaluations
Stent A				
5*	0.511	2.00	44.59	7
6	0.526	2.63	50.74	11
7	0.535	3.13	52.22	12
8	0.542	3.75	55.97	10
9	0.548	4.22	55.97	18
10	0.552	4.81	58.09	15
Stent B				
4*	0.538	2.00	61.42	6
5	0.560	2.66	68.12	15
6	0.572	3.50	79.96	9
7	0.581	4.00	77.17	9
8	0.587	4.75	82.45	9
Stent C				
4	0.582	2.09	47.13	10
6	0.611	3.88	66.69	12
8*	0.625	5.00	63.22	7
Stent D				
4 – 2:2	0.529	2.38	87.09	10
5 – 2:3	0.529	3.13	96.88	11
6 – 2:2:2	0.536	4.06	111.09	15
6 – 3:3	0.530	3.88	104.00	11
7 – 2:2:3	0.536	4.63	107.04	11
8 – 2:3:3*	0.537	5.00	97.25	7
9 – 3:3:3*	0.544	5.00	79.68	7

* Optimization converged to the boundary of the parameter space

The intrastrut area as a function of d (i.e. cell expansion curve) for a single stent cell is plotted in Figure 3.12. For the peak-to-peak stent designs (A and B), the cell expansion curve represents a concave function. This relationship is linear for the peak-to-valley design (D). As a hybrid of peak-to-peak and peak-to-valley designs, the cell expansion curve for stent C is fairly linear with a small degree of concavity. The degree of expansion for each of the optimal models is also denoted in Figure 3.12. The optimal

intrastrut angle is generally smaller for designs A, B and C (A: 50-58°, B: 68-82°, C: 47-67°) than that of design D (87-107°).

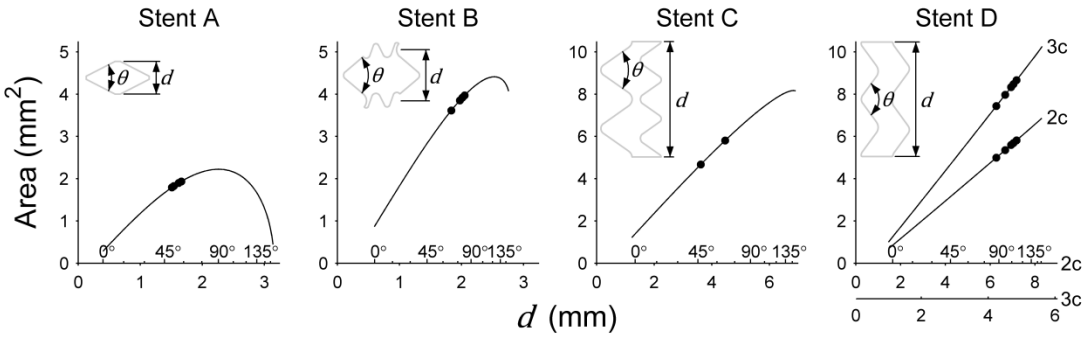

Figure 3.12: The intrastrut area relative to the parameter d (expansion curve) for a single cell of each stent design. For stent D, the expansion curves of both the two crown (2c) and three crown (3c) cells are shown. The value of *d* corresponding to the cell geometry of each optimal model is denoted along the curve as a black dot. Only configurations in which the optimization did not converge to a boundary are plotted. As an additional reference, the intrastrut angle is also denoted above the x-axis.

Plots of the design cost relative to the vessel diameter are shown in Figure 3.13. These plots can be used to identify the optimal stent configuration for any given vessel diameter. The optimal configuration is simply the curve with the minimum cost for a given vessel diameter. Similarly, an optimal vessel diameter range for each stent configuration can be estimated from the intersection of the cost function with adjacent stent configuration. For example, the cost curves for the N_C=5 and N_C=6 configurations of design A intersect at about 2.6 mm and the curves for the N_C=6 and N_C=7 configuration of design A intersect at about 3.2 mm. Thus, the optimal vessel diameter range for the N_C=6 configuration of design A is between 2.6 and 3.2 mm. The optimal vessel diameter ranges for each stent design is denoted by the alternating white and gray boxes on Figure 3.13. The 6-2:2:2, not the 6-3:3, stent design was used when computing the optimal vessel diameter range for stent design D, as this is representative of the six crown version of the commercially available Multi-Link Vision stent.

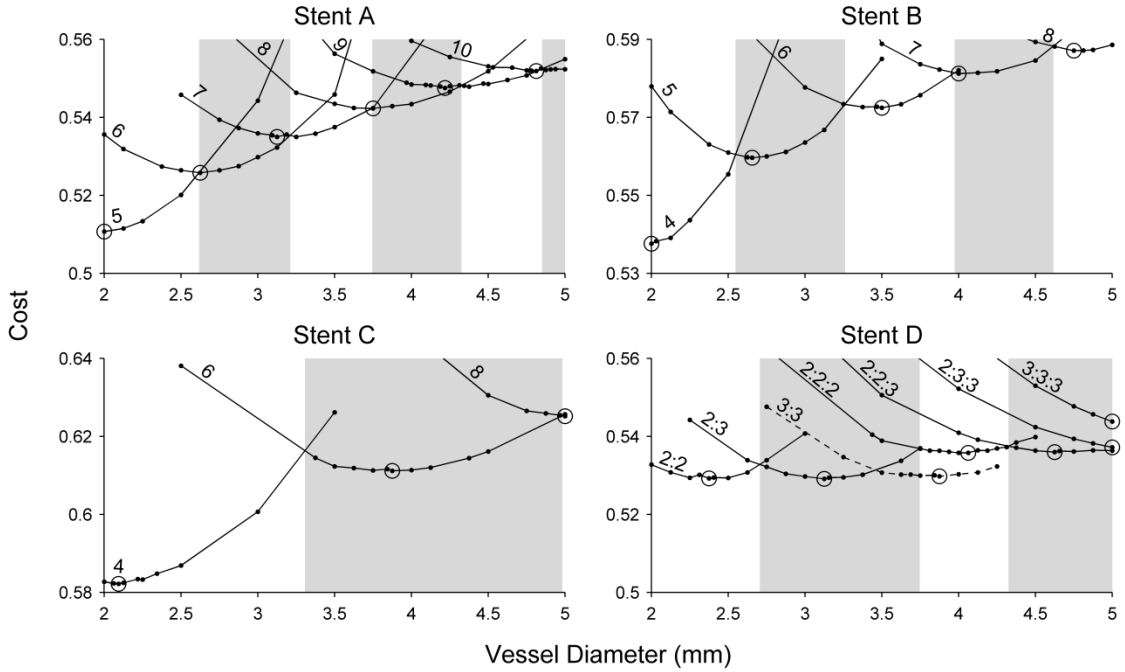

Figure 3.13: Cost function versus the vessel diameter for the various configurations of each stent design. The stent configuration, or number of circumferential crowns, is denoted above each curve. The model corresponding to the optimal vessel diameter is circled for each stent configuration. The optimal vessel diameter range for each configuration is denoted by the alternating gray and white shaded areas. Both the 3:3 and 2:2:2 configurations of stent D represent a six crown stent, but the optimal vessel diameter range was not computed for the 3:3 configuration so it is denoted with a dotted line.

Using a similar analysis, a comparison of the hemodynamic performance among the various stent designs is shown in Figure 3.14 by plotting a *least cost curve* for each design. The least cost curve is constructed by extracting the minimum possible cost from among all the configurations of a stent design for entire vessel diameter range as plotted Figure 3.14. A comparison of the least cost curves indicates that in the most hemodynamically favorable configuration, stent design C performs worse than all other stent designs regardless of vessel diameter. Stent D is the best performing commercially inspired stent design, while the generic slotted-tube stent is the best performing design in vessels less than 3.0 mm in diameter.

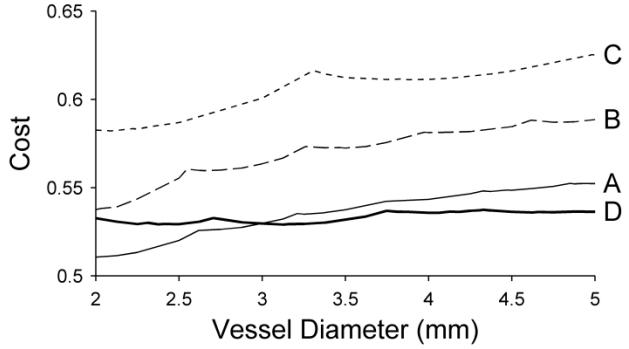

Figure 3.14: Comparison of the least cost curves of each stent design. The least cost curve represents the most best hemodynamic cost of a stent design for all vessel diameters between 2.0 and 5.0 mm in diameter.

Histograms of the normalized TAWSS over the intrastrut area for each optimal model are shown in Figure 3.15. Each histogram was constructed with a bin size of normalized TAWSS equal to 0.02. For a given stent design, the histograms of normalized TAWSS are similar for the optimal models among all configurations, thus the pattern of TAWSS is only shown for one representative stent cell. The histograms of stent designs B and C are more skewed towards lower values of TAWSS when compared to designs A and D, indicating a greatest area of low TAWSS is generated by the optimal models for these stent designs. Visual inspection of the TAWSS over the stent cell of design B illustrates a majority of the low TAWSS is localized near the connector element (Figure 3.15, Stent B dotted line). Similarly, the design of stent C produces localized areas of decreased TAWSS near connector elements as well as in the middle of the intrastrut area (Figure 3.15, Stent C dotted lines).

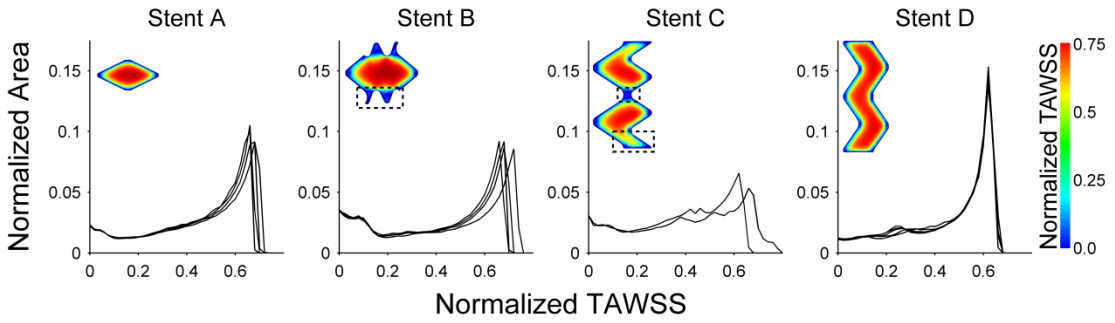

Figure 3.15: Histogram of the TAWSS over the intrastrut area of optimal stent models along with a representative pattern of TAWSS on an optimal stent geometry. Histograms are only plotted for optimizations that did not converge to a boundary. TAWSS is shown normalized to the TAWSS computed in the unstented portion of the vessel. Localized areas of low TAWSS near cell connector elements are indicated by the dotted lines for stents B and C.

Given that the designs of stents B, C and D closely resemble the commercially available BX Velocity, Express[2] and Multi-Link stents respectively, a comparison of hemodynamically optimal vessel diameter range (Figure 3.13) to that of the manufacturer's recommended diameter range is presented in Table 3.4. The expanded geometry of a single stent crown at the minimum and maximum of each range is also depicted in Figure 3.16. For any given vessel diameter, the commercial stents are configured with a greater number of crowns than the hemodynamically optimal configurations.

Table 3.4: Comparison of the vessel diameter range recommended by stent manufactures and the hemodynamically optimal vessel diameter range predicted by the CFD simulations in this investigation.

	Diameter Range (mm)		Intrastrut Angle Range (°)	
Circumferential Repetitions (N_C)	Manufacturer	Simulation Based	Manufacturer*	Simulation Based
(N/A)/A				
5		– 2.58		– 65.4
6		2.58 – 3.22		50.6 – 67.4
7		3.22 – 3.75		54.3 – 67.4
8		3.75 – 4.34		55.9 – 68.4
9		4.34 – 4.82		58.0 – 68.1
10		4.83 –		58.7 –
BX Velocity/B				
4		– 2.55		– 93.4
5		2.55 – 3.28		63.5 – 97.4
6	2.25 – 3.00	3.28 – 3.98	36.6 – 61.4	70.8 – 100.4
7	3.00 – 3.50	3.98 – 4.59	46.9 – 61.4	76.3 – 99.5
8		4.59 –		78.5 –
Express^2/C				
4		– 3.24		– 85.6
6	2.25 – 3.50	3.24 – 4.98	20.4 – 48.2	43.7 – 86.3
8	4.00 – 5.00	4.98 –	36.8 – 54.1	53.7 –
Multi-Link/D				
4 – 2:2		– 2.71		– 103.7
5 – 2:3		2.71 – 3.75		71.5 – 130.6
6 – 2:2:2	2.00 – 3.00	3.75 – 4.33	29.6 – 61.7	89.8 – 117.7
7 – 2:2:3		4.33 –		89.1 –
8 – 2:3:3				
9 – 3:3:3†	3.50 – 5.00		41.4 – 75.4	

* Manufacture's intrastrut angle was computed using the designs of stents B, C and D

† Manufacture's diameter range based on combination of Multi-Link Vision and Ultra

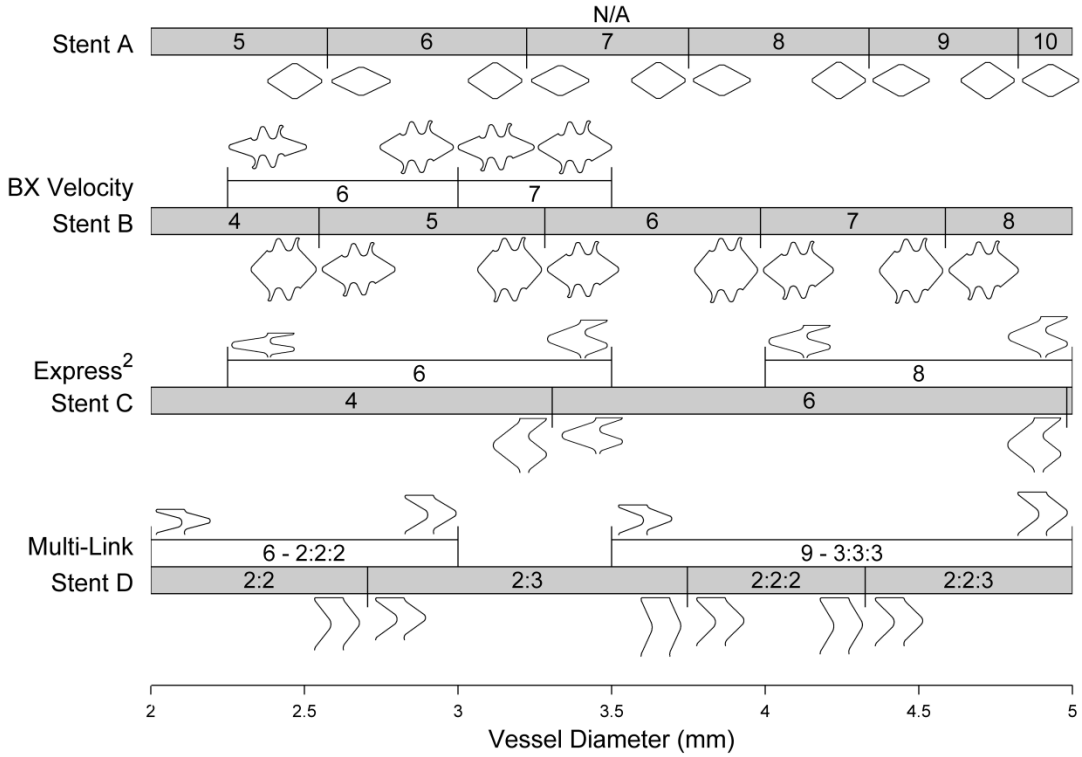

Figure 3.16: Comparison of the vessel diameter range of each commercially available stents to the hemodynamically optimal diameter configuration diameter range. The expanded geometry of a single circumferential crown corresponding to the minimum and maximum cell expansion of each range is also shown.

3.4.4 Discussion

This case study used the stent optimization method to identify the hemodynamically optimal vessel diameter for various configurations of a generic slotted-tube and three commercially available stent designs. The results indicate that current commercial stent configurations have a greater number of circumferentially repeating stent crowns than is hemodynamically optimal. Presumably a larger number of stent crowns provide a greater amount of vessel scaffolding, but the current results demonstrate that this also increases the area of the vessel exposed to potentially deleterious levels low TAWSS.

The unique framing of the optimization problem in this case study facilitated a thorough and detailed analysis of the relationship between vessel diameter and stent configuration without necessitating numerous optimizations. The main objective of the investigation was to identify the optimal value of N_C for a given stent design and vessel diameter. This naturally implies formulating the optimization problem to directly solve for the optimal value of N_C while maintaining vessel diameter constant. Instead this investigation used the reverse formulation to identify the optimal vessel diameter for a given N_C. This approach did not directly solve for N_C, but rather indirectly computed the optimal value of N_C for a given stent design and vessel diameter by examining the relationships between the cost function and vessel diameter (Figure 3.13). Moreover, the reverse formulation also enabled the analysis of the optimal intrastrut angle and quick computation of the optimal vessel diameter range for each stent configuration. The direct approach would require numerous optimizations to compute these parameters with the same accuracy achieved using the reverse formulation.

The results of this investigation confirm and extend the findings of the previous case study (Section 3.3) in which it was determined that the optimal value of N_C depended on the intrastrut angle for a generic slotted-tube stent, similar to stent A. As shown by the intrastrut angles of the optimal models (Table 3.3), the small range of optimal angles for each stent design supports the previous conclusion that the optimal value of N_C is dependent on the intrastrut angle. However, contrary to the findings of the previous study, the current results indicate that the optimal intrastrut angle is somewhat dependent on vessel size. The optimization routine generally converged to designs with a smaller intrastrut angle in small diameter vessels (Table 3.3). The discrepancy between

the findings of these studies is likely caused by the difference in design constraints used in each study. In the previous study, the intrastrut area was constrained to 1 mm^2, 2 mm^2 or 3 mm^2 and optimization were only performed with 2.25 mm and 3.0 mm diameter vessels. The current results were obtained by constraining the stent strut dimensions and allowing the vessel diameter, and subsequently the intrastrut area, to vary. These constraints mimic the realistic deployment of a stent and result in a better approximation of the optimal intrastrut angle. Thus the optimal intrastrut angle for a slotted-tube design is likely between 50° and 60°, as opposed to the previously reported value of 40°.

There was a large difference in the optimal intrastrut angle observed between various stent designs. The optimal intrastrut angle for peak-to-peak (A and B) and hybrid (C) designs was smaller than that of the peak-to-valley design (D). Based on the hypothesis that the optimal stent design represents a balance between progressive strut misalignment and increasing intrastrut area, this finding is likely explained by the nonlinear relationship between the intrastrut area and the vessel diameter for stent designs A, B and C (Figure 3.12). Unlike the linear relationship of peak-to-valley designs, the rate of increase in intrastrut area decreases with increasing stent diameter for peak-to-peak and hybrid designs, resulting in a smaller optimal intrastrut angle. This is most evident for designs A and B, in which the cell geometry of each optimal model corresponds to a similar location on the cell expansion curve slightly less than the possible maximum cell area.

The present findings indicate the cost of the models corresponding to the optimal vessel diameter of a given stent configuration increases with increasing vessel diameter and N_C for designs A, B and C. This relationship causes the value of the optimal vessel

diameter to be skewed towards the low end, or fall completely outside of the optimal vessel diameter range for most configurations (Figure 3.13). For example, the optimal vessel diameter for the N_C=7 configuration of design B is 4.00 mm, while the optimal vessel diameter range of this configuration is about 4.00-4.60 mm. The lack of this trend in stent D likely arises from the combined use of two and three crest cell geometries. Incorporating a three cell geometry into the stent configuration generally resulted in lower costs than the two crest cell design as evident by comparison of the 6-2:2:2 and 6-3:3 optimization (Figure 3.13). Although the two stent designs have the same number of crowns, the 6-3:3 stent has a lower associated cost (0.536 vs. 0.530).

The least cost curves (Figure 3.14) and TAWSS distributions (Figure 3.15) both suggest that the relative ranking of performance (best to worst) of the commercially inspired stent designs considered is D (Multi-Link), B (BX Velocity) and C (Express^2). It should be noted that some commercial versions of Stent D include a flexible connector link that would likely produced a greater area of low TAWSS than was computed here which may affect this ranking. While these rankings provide insight to relative performance of commercial stents, they cannot be used to draw any general conclusions about the performance of peak-to-peak, peak-to-valley or hybrid designs as the strut thickness and width was selected among the stent designs to mimic the dimensions of the commercially available equivalents. This investigation also highlights the superior adaptability of the peak-to-peak and peak-to-valley designs to various vessel diameters as compared to the hybrid design (Figure 3.16). The number of circumferential crowns of the hybrid design can only be incremented by a factor of two due to the cell geometry, whereas the other designs allow for unit increments.

Compared to configurations of commercially available stents, the current results suggest that hemodynamically optimal stents contain fewer circumferentially repeating crowns, which results in greater spacing between struts. While an increase in strut spacing is hemodynamically advantageous, this may adversely affect other stent design criteria. Specifically, increasing strut spacing imposes higher focal mechanical stresses on the artery and may reduce the radial strength of the stent [10]. For DES stents, increased strut spacing reduces the uniformity of drug release along with the intrastrut drug concentration [45]. Interestingly, a previous study by Iakovou *et al.* demonstrated that increased strut spacing was not associated with unfavorable clinical outcomes for the Cypher stent, the DES version of the BX Velocity [31, 35, 88, 93, 100]. In this study six crown Cypher stents were overdilated beyond the suggested 3.0 mm diameter maximum for 3.5-4.0 diameter vessels, similar to the hemodynamically optimal vessel range for this stent configuration. Overdilation was not associated with increased late lumen loss or binary restenosis rate. However, this study was only performed in large diameter vessels which are generally associated with a decreased rate of restenosis and is unclear if these results would translate to smaller vessels. Similarly, overexpansion of the Express^2 and Multi-Link designs has not been studied in detail.

3.5 Discussion of the optimization methods

3.5.1 Summary

Stent design and geometry are known to influence clinical outcomes including endothelialization and restenosis after DES and BMS implantation, respectively [11, 40, 60-62], but previous studies have largely employed a “trial-and-error” approach to improving stent design. This works represents the first investigation to use a

computationally efficient method for optimizing cardiovascular stent design in unsteady flow using CFD.

The cost function used in the optimization routine measured the disparity in TAWSS between the stented region and unstented region. While this cost function is representative of the well-establish concept of WSS homeostasis, the actual value of this index has not previously been studied or correlated to vascular disease. Other CFD studies have used a critical value of 4 or 5 dynes/cm^2 as the threshold of low WSS [54], as it has been correlated to intimal thickening [39, 66, 70, 86]. However, using a threshold may not be able to differentiate between device designs in flow environments with excessively high or low WSS. The cost function used in this investigation is more versatile than a thresholding cost function and capable of discriminating between stent designs regardless of flow environment, which was most evident in Case Study 2. The magnitude of WSS varied greatly among these models since the inflow rate was kept constant for a wide range of vessel diameters. Because the TAWSS in the stented region of the model was normalized to TAWSS in an unstented region of the vessel, the formulation of the cost function was not dependent of vessel diameter.

In the current investigation, only the magnitude of TAWSS was considered as a determinant of the optimal stent design. Although low TAWSS is the most commonly studied index for predicting in-stent restenosis, several researchers postulate that oscillatory shear index, spatial or temporal wall shear-stress gradients, and wall shear stress angle gradients may also be useful indices for predicting restenosis [8]. The current optimization methodology could be adapted to perform multi-objective optimization [119] in order to include the effects of other hemodynamic indices in future studies. For

example, Yang *et al.* recently implemented multi-objective optimization with regard to energy efficiency and WSS to determine the optimal a shape for a Fontan surgical design which is performed on patients with single ventricle heart defects [57].

3.5.2 Limitations

The present results should be interpreted within the constraints of several potential limitations. Each coronary vessel was modeled as an ideal cylinder which likely does not represent the actual vessel geometry following stent deployment. As discussed earlier (Section 2.1), a finite element simulation of the stent expansion may be the best method for determining the expanded geometry of the stent and vessel, but this approach would further increase the computational cost of the already computationally expensive optimization routine and therefore was not pursued in this investigation. Though the previously described patient-specific model of a coronary bifurcation employed a deformable wall model (Section 2.4.1), the vessel models in this investigation employed a rigid wall assumption for all CFD simulations for simplicity and increased computational efficiency. Since the compliance of stented arteries has been shown to be nearly zero, a rigid wall assumption is likely valid within the stented region that is quantified during the optimization routine [95, 96].

The current optimization method does not consider uncertainty in simulation or model inputs (i.e. model inflow waveform, boundary conditions, blood rheology, stent-to-artery ratio, etc.) that may affect the optimization output. As an example, the influence of the inflow waveform was analyzed by recomputing the optimal diameter of stent design A with N_C=6 using a steady inflow instead of a pulsatile waveform. The optimization converged to the same vessel diameter for both inlet boundary conditions,

but the cost was lower for the steady inflow condition when comparing models of equal vessel diameter (Figure 3.17). This analysis suggests the design cost is sensitive to the contour of the inflow waveform, but the inflow does not affect the optimal design parameters. Unfortunately it is tough to elicit a definitive relationship between the inflow and cost since only two inflow cases were examined. It is also unknown if the relationship between the inflow and cost would be similar for all of the stent designs and the entire range of vessel diameters studied here. These potential differences in the cost due to the inflow may affect the computed optimal vessel diameters (Figure 3.13) and relatively ranking of the stent designs (Figure 3.14). Thus, each of the optimizations in this investigation used a pulsatile inflow similar to a human coronary waveform for increased physiologic realism and to reduce the potential influence of a steady inflow. This analysis of the model inflow underscores the difficulty in understanding the potential influence of possible input variables. Future studies that implement robust optimization techniques may provide a better understanding of the sensitivity of output parameters to input uncertainties [19].

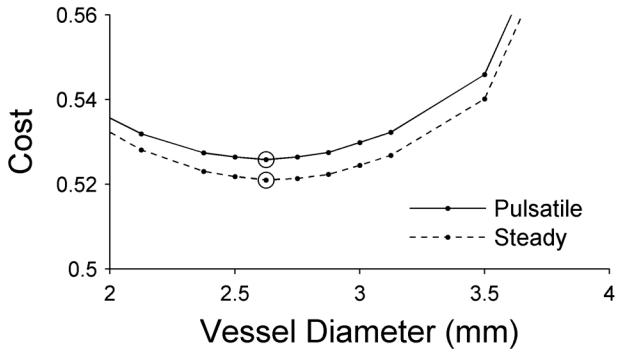

Figure 3.17: The cost function versus the vessel diameter for the stent B (N_C=6) when a steady and a pulsatile inflow is applied to the CFD model. The model corresponding to the optimal vessel diameter is circles on each plot.

In the first part of this thesis (Chapter 2), the computational mesh of each stented model was scrutinized to ensure mesh independence by comparing WSS between successive meshes with increasing mesh densities. This analysis was not included in the optimization routine since it usually required three to five mesh refinements to reach mesh independence, and the process of successive mesh refinements would drastically increase the computational expense of the optimization routine. Instead mesh independence was investigated by computing the optimal vessel diameter of stent design B with N_C=5 using two different mesh densities. The anisotropic mesh generation parameters were tailored to create meshes with roughly 3-4 and 6-8 million elements for this stent configuration. The optimization converged to a vessel diameter of 2.625 mm when high density meshes were used compared to 2.65625 mm for the low density meshes (Figure 3.18). In general, the cost of stented models was slightly increased for models with a higher mesh density, but the relative difference in cost was <1% between models with an equal vessel diameter. Since doubling the mesh size only resulted in small variations in the computed cost and the optimal vessel diameter, the optimization results were assumed to be independent of the computational mesh for the relatively low density meshes. The meshing parameters used to generate 3-4 million element meshes were used throughout the entire investigation.

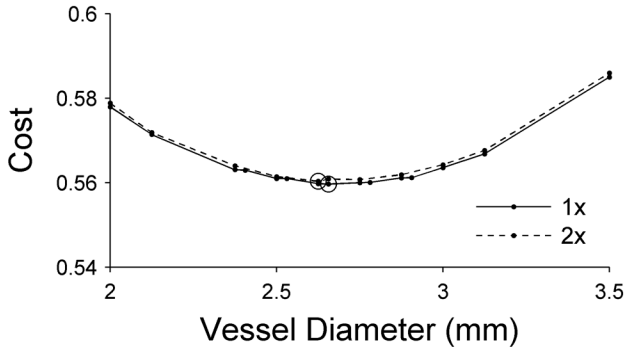

Figure 3.18: The cost function versus the vessel diameter for the stent B (N_C =5) for computational meshes with a density of 3-4 million elements (1x) and 6-8 million elements (2x).

This work attempted to include some of the most widely used stents geometries at this time. The companies referred to here may now have, or be developing, newer stents for which the demonstrated optimization techniques could be used to identify the hemodynamically optimal designs configurations. The current results do describe some general hemodynamic characteristics of peak-to-peak, peak-to-valley stent and hybrid designs which are likely applicable to new designs without a complete optimization analysis. However, the variability among designs within these categories, as shown by the difference in optimal configurations of stents A and B (Table 3.3 and Figure 3.16), suggests a complete optimization analysis is necessary for each unique stent design.

3.6 Conclusion

In summary, the current investigation describes an efficient optimization framework that uses 3D CFD coupled with a derivative-free optimization routine to indentify hemodynamically optimal stents. The method was applied to analyze the optimal number of circumferentially repeating stents cells and intrastrut angle that minimize the area of low TAWSS for various stent designs. In general, the results

indicate that commercial stent designs incorporate a greater number of circumferentially repeating stent crowns than is hemodynamically optimal, which may subject the vessel to potential deleterious levels of low TAWSS and may partially explain why rates of restenosis remain high after stent implantation in small diameter vessels. Incorporating the results of this investigation in future stent designs may improve endothelialization after DES and reduce neointimal hyperplasia and subsequent restenosis after BMS.

Chapter 4

Future Directions and Conclusion

4.1 Future computational investigations

The findings of the optimization case studies would be particularly interesting when coupled with additional solid mechanics, deliverability and drug-elution analyses often considered when designing a stent. In this investigation, the parsimonious choice of stent parameters ensured the optimization did not pursue infeasible stent designs. This resulted in only one stent or vessel parameter varying during each optimization, but the SMF optimization algorithm is fully capable of considering multiple design parameters [13, 64, 120]. Implementing a multi-objective optimization that considers additional, non-hemodynamic design criteria would enable additional design parameters to be optimized. For example, optimizing the strut thickness from a purely hemodynamic perspective produces an optimal stent design with a negligible thickness. However, if the radial strength of the stent was also considered, the competing solid mechanic and hemodynamic effects of reducing strut thickness would prevent the optimization from converging on an infeasible design. Additional solid mechanics design criteria might also include the compliance and stress induced on the arterial wall which are known to be influenced by strut thickness and intrastrut area [9, 31]. In designing DES, smaller

intrastrut areas that promote uniform drug distribution are favorable since non-uniform drug concentrations resulting from stent geometry or overlapping stents have previously been shown to suppress re-endothialization atop stent struts [8, 119]. As discussed earlier, the SMF optimization technique can be adapted to perform multi-objective optimization [92], which would enable a thorough analysis of the trade-offs between hemodynamic indices the other design criteria. Therefore the largest obstacle to considering additional design criteria within the optimization routine is incorporating additional numerical analyses, such as FEA or drug advection-diffusion, into the optimization framework.

The optimization methodology presented here was developed to understand the relationship between stent configuration and vessel diameter, and possibly improve stent design for treating small vessel lesions. With a few modifications, this methodology could be used to investigate potential design improvements for treating other difficult lesions subsets such as those in the left main coronary artery where efficacy data for most stents is limited and local disruptions in the vicinity of the bifurcation increases the potential for flow patterns linked neointimal growth and thrombus formation [58]. Additionally, the optimization method could be coupled with the patient-specific stenting method (Chapter 2) to determine the optimal stent designs for individual patients. Determining the optimal geometry of the flow diverting cerebral stent (Section 2.5) would be a particularly interesting application for the optimization method.

4.2 Validation of optimization results with animal models

The application of the stent optimization method generally indicate that decreasing the number of circumferentially repeating stent crowns of commercially available stent designs would subsequently reduce neointimal growth and promote the

endothelialization of strut. To be clinical relevant, this finding needs to be validated with an animal model. LaDisa *et al*. developed a technique for implanting stents in rabbit iliac arteries [63], which was later used to correlate low WSS with increased neointimal hyperplasia . Using the computed optimal vessel diameter range for various stent configurations (Figure 3.16) as a guide, the stent implantation method could be used to implant stents with the optimal, less than optimal and greater than optimal number of circumferential repeating stent crowns depending on the measured diameter of the rabbit artery. The rabbits would then be euthanized after 21-28 days to quantify the amount neointimal hyperplasia within each experimental group, thereby validating the results of the CFD based optimization. With the addition of medical imaging, the subject-specific stenting methods could be also used to generate a model of the flow domain for each rabbit following stent implantation.

4.3 Conclusion

The computational techniques for evaluating cardiovascular stent designs described in this thesis constitute a substantial improvement over previous CFD studies of stent design. Previous studies have largely relied on simple vessel and stent geometries to described hemodynamic alterations in response to coronary stent implantation. Therefore, the method of virtually implanting commercial stents into patient-specific vessel geometries (Chapter 2) represents a necessary advancement in stent modeling techniques to further understand hemodynamics in complex coronary lesions geometries (e.g. bifurcation lesions) that remain difficult to treat and to evaluate emerging applications of stent implantation (e.g. flow-diverting stents). To the author's knowledge this is also the first investigation to couple an optimization algorithm 3D CFD to

determine hemodynamically optimal stent designs (Chapter 3). Collectively, these methods provide a means of systematically evaluating and improving the hemodynamic performance of current and next-generation stents. Moreover, these methods can be used to avoid the costly trial-and-error approach to stent design that has often been used in the past.

REFERENCES

[1] Alderson H, Zamir M. Effects of stent stiffness on local haemodynamics with particular reference to wave reflections. *J Biomech*, 2004;**37**:339-48.

[2] Antiga L, Steinman DA. Robust and objective decomposition and mapping of bifurcating vessels. *IEEE Trans Med Imaging*, 2004;**23**(6):704-13.

[3] Appanaboyina S, Mut F, LÃ¶hner R*, et al.* Computational fluid dynamics of stented intracranial aneurysms using adaptive embedded unstructured grids. *Int J Numer Meth Fluids*, 2008;**57**(5):475-493.

[4] Arquizan C, Trinquart L, Touboul PJ*, et al.* Restenosis is more frequent after carotid stenting than after endarterectomy: the EVA-3S study. *Stroke*, 2011;**42**:1015-20.

[5] Arts T, Kruger RT, van Gerven W*, et al.* Propagation velocity and reflection of pressure waves in the canine coronary artery. *Am J Physiol*, 1979;**237**(4):H469-74.

[6] Atherton MA, Bates RA. Robust optimization of cardiovascular stents: a comparison of methods. *Engineering Optimization*, 2004;**36**:207 - 217.

[7] Audet C, Dennis JJE. Mesh Adaptive Direct Search Algorithms for Constrained Optimization. *SIAM Journal on Optimization*, 2006;**17**:188-217.

[8] Audet C, Dennis JJE. A Pattern Search Filter Method for Nonlinear Programming without Derivatives. *SIAM Journal on Optimization*, 2004;**14**:980-1010.

[9] Balakrishnan B, Tzafriri AR, Seifert P*, et al.* Strut position, blood flow, and drug deposition: implications for single and overlapping drug-eluting stents. *Circulation*, 2005;**111**:2958-65.

[10] Balakrishnan B, Tzafriri AR, Seifert P*, et al.* Strut position, blood flow, and drug deposition: implications for single and overlapping drug-eluting stents. *Circulation*, 2005;**111**(22):2958-65.

[11] Balossino R, Gervaso F, Migliavacca F*, et al.* Effects of different stent designs on local hemodynamics in stented arteries. *J Biomech*, 2008;**41**:1053-61.

[12] Baráth K, Cassot F, Fasel JH*, et al.* Influence of stent properties on the alteration of cerebral intra-aneurysmal haemodynamics: flow quantification in elastic sidewall aneurysm models. *Neurol Res*, 2005;**27 Suppl 1**:S120-8.

[13] Bedoya J, Meyer CA, Timmins LH*, et al.* Effects of stent design parameters on normal artery wall mechanics. *J Biomech Eng*, 2006;**128**:757-65.

[14] Benndorf G, Ionescu M, Valdivia y Alvarado M*, et al.* Anomalous hemodynamic effects of a self-expanding intracranial stent: comparing in-vitro and ex-vivo models using ultra-high resolution microCT based CFD. *J Biomech*, 2010;**43**(4):740-8.

[15] Berry JL, Manoach E, Mekkaoui C*, et al.* Hemodynamics and wall mechanics of a compliance matching stent: in vitro and in vivo analysis. *J Vasc Interv Radiol*, 2002;**13**:97-105.

[16] Berry JL, Santamarina A, Moore JE*, et al.* Experimental and computational flow evaluation of coronary stents. *Ann Biomed Eng*, 2000;**28**:386-98.

[17] Bishop RL. There is more than one way to frame a curve. *The American Mathematical Monthly*, 1975;**82**:246-251.

[18] Blouza A, Dumas L, M'Baye IC. Multiobjective optimization of a stent in a fluid-structure context. *Proceedings of the 2008 GECCO conference companion on Genetic and evolutionary computation*, 2008:2055-2060.

[19] Booker AJ, Dennis JE, Frank PD*, et al.* A rigorous framework for optimization of expensive functions by surrogates. *Structural and Multidisciplinary Optimization*, 1999;**17**:1-13.

[20] Bosiers M, Cagiannos C, Deloose K*, et al.* Drug-eluting stents in the management of peripheral arterial disease. *Vasc Health Risk Manag*, 2008;**4**:553-9.

[21] Cortese B, Bertoletti A, De Matteis S*, et al.* Drug-eluting stents perform better than bare metal stents in small coronary vessels: A meta-analysis of randomised and observational clinical studies with mid-term follow up. *Int J Cardiol*, 2011.

[22] D'Urso PI, Lanzino G, Cloft HJ*, et al.* Flow diversion for intracranial aneurysms: a review. *Stroke*, 2011;**42**:2363-8.

[23] Doyle B, Rihal CS, O'Sullivan CJ*, et al.* Outcomes of stent thrombosis and restenosis during extended follow-up of patients treated with bare-metal coronary stents. *Circulation*, 2007;**116**:2391-8.

[24] Duraiswamy N, Cesar JM, Schoephoerster RT*, et al.* Effects of stent geometry on local flow dynamics and resulting platelet deposition in an in vitro model. *Biorheology*, 2008;**45**:547-61.

[25] Ebrahimi N, Claus B, Lee CY*, et al.* Stent conformity in curved vascular models with simulated aneurysm necks using flat-panel CT: an in vitro study. *AJNR Am J Neuroradiol*, 2007;**28**(5):823-9.

[26] Elezi S, Kastrati A, Neumann FJ*, et al.* Vessel size and long-term outcome after coronary stent placement. *Circulation*, 1998;**98**:1875-80.

[27] Ellwein L, Otake H, Gundert T*, et al.* Optical Coherence Tomography for Patient-specific 3D Artery Reconstruction and Evaluation of Wall Shear Stress in a Left Circumflex Coronary Artery. *Cardiovascular Engineering and Technology*:1-16.

[28] Epstein AJ, Polsky D, Yang F*, et al.* Coronary revascularization trends in the United States, 2001-2008. *JAMA*, 2011;**305**(17):1769-76.

[29] Farb A, Burke AP, Kolodgie FD*, et al.* Pathological mechanisms of fatal late coronary stent thrombosis in humans. *Circulation*, 2003;**108**:1701-6.

[30] Finet G, Gilard M, Perrenot B*, et al.* Fractal geometry of arterial coronary bifurcations: a quantitative coronary angiography and intravascular ultrasound analysis. *EuroIntervention*, 2007;**3**:490-98.

[31] Finn AV, Kolodgie FD, Harnek J*, et al.* Differential response of delayed healing and persistent inflammation at sites of overlapping sirolimus- or paclitaxel-eluting stents. *Circulation*, 2005;**112**:270-8.

[32] Finn AV, Nakazawa G, Joner M*, et al.* Vascular responses to drug eluting stents: importance of delayed healing. *Arterioscler Thromb Vasc Biol*, 2007;**27**:1500-10.

[33] Ford MD, Alperin N, Lee SH*, et al.* Characterization of volumetric flow rate waveforms in the normal internal carotid and vertebral arteries. *Physiol Meas*, 2005;**26**:477-88.

[34] Gander W, Golub GH, Strebel R. Least-squares fitting of circles and ellipses. *BIT Numerical Mathematics*, 1994;**34**:558-578.

[35] Garasic JM, Edelman ER, Squire JC*, et al.* Stent and artery geometry determine intimal thickening independent of arterial injury. *Circulation*, 2000;**101**:812-8.

[36] Glagov S, Weisenberg E, Zarins CK*, et al.* Compensatory enlargement of human atherosclerotic coronary arteries. *N Engl J Med*, 1987;**316**:1371-5.

[37] Hanson AJ, Ma H. Parallel transport approach to curve framing. *Indiana University, Techreports-TR425*, 1995;**11**:3-7.

[38] Hashimoto T, Meng H, Young WLCP. Intracranial aneurysms: links among inflammation, hemodynamics and vascular remodeling. *Neurol Res*, 2006;**28**:372-80.

[39] He X, Ku DN. Pulsatile flow in the human left coronary artery bifurcation: average conditions. *J Biomech Eng*, 1996;**118**:74-82.

[40] He Y, Duraiswamy N, Frank AO*, et al.* Blood flow in stented arteries: a parametric comparison of strut design patterns in three dimensions. *J Biomech Eng*, 2005;**127**:637-47.

[41] Hoi Y, Meng H, Woodward SH*, et al.* Effects of arterial geometry on aneurysm growth: three-dimensional computational fluid dynamics study. *J Neurosurg*, 2004;**101**:676-81.

[42] Hsieh IC, Chien CC, Chang HJ*, et al.* Acute and long-term outcomes of stenting in coronary vessel > 3.0 mm, 3.0-2.5 mm, and < 2.5 mm. *Catheter Cardiovasc Interv*, 2001;**53**:314-22.

[43] Hsu SW, Chaloupka JC, Feekes JA*, et al.* In vitro studies of the neuroform microstent using transparent human intracranial arteries. *AJNR*, 2006;**27**(5):1135-9.

[44] Iakovou I, Schmidt T, Bonizzoni E*, et al.* Incidence, predictors, and outcome of thrombosis after successful implantation of drug-eluting stents. *JAMA*, 2005;**293**(17):2126-30.

[45] Iakovou I, Stankovic G, Montorfano M*, et al.* Is overdilatation of 3.0 mm sirolimus-eluting stent associated with a higher restenosis rate? *Catheter Cardiovasc Interv*, 2005;**64**:129-33.

[46] Joner M, Nakazawa G, Finn AV*, et al.* Endothelial cell recovery between comparator polymer-based drug-eluting stents. *JACC*, 2008;**52**:333-42.

[47] Kamiya A, Togawa T. Adaptive regulation of wall shear stress to flow change in the canine carotid artery. *Am J Physiol*, 1980;**239**:H14-21.

[48] Kastrati A, Dibra A, Eberle S*, et al.* Sirolimus-eluting stents vs paclitaxel-eluting stents in patients with coronary artery disease: meta-analysis of randomized trials. *JAMA*, 2005;**294**:819-25.

[49] Kastrati A, Dibra A, Mehilli J*, et al.* Predictive factors of restenosis after coronary implantation of sirolimus- or paclitaxel-eluting stents. *Circulation*, 2006;**113**:2293-300.

[50] Katritsis D, Kaiktsis L, Chaniotis A*, et al.* Wall shear stress: theoretical considerations and methods of measurement. *Prog Cardio Dis*, 2007;**49**:307-29.

[51] Kim M, Levy EI, Meng H*, et al.* Quantification of hemodynamic changes induced by virtual placement of multiple stents across a wide-necked basilar trunk aneurysm. *Neurosurgery*, 2007;**61**:1305-12; discussion 1312-3.

[52] Kim M, Taulbee DB, Tremmel M*, et al.* Comparison of two stents in modifying cerebral aneurysm hemodynamics. *Ann Biomed Eng*, 2008;**36**(5):726-41.

[53] Klocke FJ, Mates RE, Canty JM, Jr.*, et al.* Coronary pressure-flow relationships. Controversial issues and probable implications. *Circ Res*, 1985;**56**(3):310-23.

[54] Ku DN, Giddens DP, Zarins CK*, et al.* Pulsatile flow and atherosclerosis in the human carotid bifurcation. Positive correlation between plaque location and low oscillating shear stress. *Arteriosclerosis*, 1985;**5**:293-302.

[55] Kuchulakanti PK, Chu WW, Torguson R*, et al.* Correlates and long-term outcomes of angiographically proven stent thrombosis with sirolimus- and paclitaxel-eluting stents. *Circulation*, 2006;**113**:1108-13.

[56] LaDisa JF, Guler I, Olson LE*, et al.* Three-dimensional computational fluid dynamics modeling of alterations in coronary wall shear stress produced by stent implantation. *Ann Biomed Eng*, 2003;**31**:972-80.

[57] LaDisa JF, Hettrick DA, Olson LE*, et al.* Stent implantation alters coronary artery hemodynamics and wall shear stress during maximal vasodilation. *J Appl Physiol*, 2002;**93**:1939-46.

[58] LaDisa JF, Jr., Meier HT, Olson LE*, et al.* Antegrade iliac artery stent implantation for the temporal and spatial examination of stent-induced neointimal hyperplasia and alterations in regional fluid dynamics. *J Pharmacol Toxicol Methods*, 2005;**51**(2):115-21.

[59] LaDisa JF, Jr., Olson LE, Douglas HA*, et al.* Alterations in regional vascular geometry produced by theoretical stent implantation influence distributions of wall shear stress: analysis of a curved coronary artery using 3D computational fluid dynamics modeling. *Biomed Eng Online*, 2006;**5**:40.

[60] LaDisa JF, Olson LE, Guler I*, et al.* Stent design properties and deployment ratio influence indexes of wall shear stress: a three-dimensional computational fluid dynamics investigation within a normal artery. *J Appl Physiol*, 2004;**97**:424-30.

[61] LaDisa JF, Olson LE, Guler I*, et al.* Circumferential vascular deformation after stent implantation alters wall shear stress evaluated with time-dependent 3D computational fluid dynamics models. *J Appl Physiol*, 2005;**98**:947-57.

[62] LaDisa JF, Olson LE, Hettrick DA*, et al.* Axial stent strut angle influences wall shear stress after stent implantation: analysis using 3D computational fluid dynamics models of stent foreshortening. *Biomed Eng Online*, 2005;**4**:59.

[63] LaDisa JF, Olson LE, Molthen RC*, et al.* Alterations in wall shear stress predict sites of neointimal hyperplasia after stent implantation in rabbit iliac arteries. *Am J Physiol Heart Circ Physiol*, 2005;**288**:H2465-75.

[64] Lally C, Dolan F, Prendergast PJ. Cardiovascular stent design and vessel stresses: a finite element analysis. *J Biomech*, 2005;**38**:1574-81.

[65] Laskey WK, Parker HG, Ferrari VA*, et al.* Estimation of total systemic arterial compliance in humans. *J Appl Physiol*, 1990;**69**:112-9.

[66] Lei M, Kleinstreuer C, Truskey GA. A focal stress gradient-dependent mass transfer mechanism for atherogenesis in branching arteries. *Med Eng Phys*, 1996;**18**:326-32.

[67] Lemos PA, Serruys PW, van Domburg RT*, et al.* Unrestricted utilization of sirolimus-eluting stents compared with conventional bare stent implantation in the "real world": the Rapamycin-Eluting Stent Evaluated At Rotterdam Cardiology Hospital (RESEARCH) registry. *Circulation*, 2004;**109**:190-5.

[68] Lieber BB, Livescu V, Hopkins LN*, et al.* Particle image velocimetry assessment of stent design influence on intra-aneurysmal flow. *Ann Biomed Eng*, 2002;**30**:768-77.

[69] Lloyd-Jones D, Adams R, Carnethon M*, et al.* Heart disease and stroke statistics--2009 update: a report from the American Heart Association Statistics Committee and Stroke Statistics Subcommittee. *Circulation*, 2009;**119**:480-6.

[70] Longest PW, Kleinstreuer C. Computational haemodynamics analysis and comparison study of arterio-venous grafts. *J Med Eng Technol*, 2000;**24**:102-10.

[71] Lonyai A, Dubin AM, Feinstein JA*, et al.* New insights into pacemaker lead-induced venous occlusion: simulation-based investigation of alterations in venous biomechanics. *Cardiovasc Eng*, 2010;**10**:84-90.

[72] Lophaven Sr, Nielsen H, SÃ¸ndergaard J. DACE - A MATLAB Kriging Toolbox version 2.0,Â Technical Report IMM-TR-2002-12. Copenhagen: Technical University of Denmark, 2002.

[73] Marsden AL, Feinstein JA, Taylor CA. A computational framework for derivative-free optimization of cardiovascular geometries. *CMAME*, 2008;**197**:1890-1905.

[74] Mauri L, Silbaugh TS, Wolf RE*, et al.* Long-term clinical outcomes after drug-eluting and bare-metal stenting in Massachusetts. *Circulation*, 2008;**118**:1817-27.

[75] McKay MD, Beckman RJ, Conover WJ. A comparison of three methods for selecting values of input variables in the analysis of output from a computer code. *Technometrics*, 1979:239-245.

[76] McLean DR, Eiger NL. Stent design: implications for restenosis. *Rev Cardiovasc Med*, 2002;**3 Suppl 5**:S16-22.

[77] Meng H, Metaxa E, Gao L*, et al.* Progressive aneurysm development following hemodynamic insult. *Journal of Neurosurgery*, 2011;**114**(4):1095-1103.

[78] Meng H, Wang Z, Kim M*, et al.* Saccular aneurysms on straight and curved vessels are subject to different hemodynamics: implications of intravascular stenting. *AJNR*, 2006;**27**:1861-5.

[79] Molyneux A, Kerr R, Stratton I*, et al.* International Subarachnoid Aneurysm Trial (ISAT) of neurosurgical clipping versus endovascular coiling in 2143 patients with ruptured intracranial aneurysms: a randomized trial. *J Stroke Cerebrovasc Dis*, 2002;**11**(6):304-14.

[80] Moore J, Berry JL. Fluid and solid mechanical implications of vascular stenting. *Ann Biomed Eng*, 2002;**30**:498-508.

[81] Morice MC. Stenting for Small Coronary Vessels. *J Invasive Cardiol*, 2003;**15**:377-379.

[82] Mortenson ME. *Geometric modeling*: Wiley New York et al., 1997.

[83] Mortier P, Van Loo D, De Beule M*, et al.* Comparison of drug-eluting stent cell size using micro-CT: important data for bifurcation stent selection. *EuroIntervention*, 2008;**4**:391-6.

[84] Muller J, Sahni O, Li X*, et al.* Anisotropic adaptive finite element method for modelling blood flow. *Comp Meth Biomech Biomed Engin*, 2005;**8**(5):295-305.

[85] Murphy J, Boyle F. Assessment of the effects of increasing levels of physiological realism in the computational fluid dynamics analyses of implanted coronary stents. *Conf Proc IEEE Eng Med Biol Soc*, 2008;**2008**:5906-9.

[86] Murphy JB, Boyle FJ. A full-range, multi-variable, CFD-based methodology to identify abnormal near-wall hemodynamics in a stented coronary artery. *Biorheology*, 2010;**47**(2):117-32.

[87] Myers JG, Moore JA, Ojha M*, et al.* Factors influencing blood flow patterns in the human right coronary artery. *Ann Biomed Eng*, 2001;**29**(2):109-20.

[88] Pache J, Kastrati A, Mehilli J*, et al.* Intracoronary stenting and angiographic results: strut thickness effect on restenosis outcome (ISAR-STEREO-2) trial. *JACC*, 2003;**41**:1283-8.

[89] Perry R, De Pasquale CG, Chew DP*, et al.* Changes in left anterior descending coronary artery wall thickness detected by high resolution transthoracic echocardiography. *Am J Cardiol*, 2008;**101**(7):937-40.

[90] Pflederer T, Ludwig J, Ropers D*, et al.* Measurement of coronary artery bifurcation angles by multidetector computed tomography. *Invest Radiol*, 2006;**41**(11):793-8.

[91] Radaelli AG, Augsburger L, Cebral JR*, et al.* Reproducibility of haemodynamical simulations in a subject-specific stented aneurysm model--a report on the Virtual Intracranial Stenting Challenge 2007. *J Biomech*, 2008;**41**(10):2069-81.

[92] Ragosta M, Dee S, Sarembock IJ*, et al.* Prevalence of unfavorable angiographic characteristics for percutaneous intervention in patients with unprotected left main coronary artery disease. *Catheter Cardiovasc Interv*, 2006;**68**(3):357-62.

[93] Rogers C, Edelman ER. Endovascular stent design dictates experimental restenosis and thrombosis. *Circulation*, 1995;**91**:2995-3001.

[94] Sadasivan C, Cesar L, Seong J*, et al.* An original flow diversion device for the treatment of intracranial aneurysms: evaluation in the rabbit elastase-induced model. *Stroke*, 2009;**40**:952-8.

[95] Sankaran S, Audet C, Marsden AL. A method for stochastic constrained optimization using derivative-free surrogate pattern search and collocation. *Journal of Computational Physics*, 2010;**229**(12):4664-4682.

[96] Sankaran S, Marsden AL. A stochastic collocation method for uncertainty quantification and propagation in cardiovascular simulations. *J Biomech Eng*, 2011;**133**(3):031001.

[97] Sedat J, Chau Y, Mondot L*, et al.* Endovascular occlusion of intracranial wide-necked aneurysms with stenting (Neuroform) and coiling: mid-term and long-term results. *Neuroradiology*, 2009;**51**(6):401-9.

[98] Sharma SK, Sweeny J, Kini AS. Coronary bifurcation lesions: a current update. *Cardiol Clin*, 2010;**28**(1):55-70.

[99] Sniderman KW. Noncoronary vascular stenting. *Prog Cardiovasc Dis*, 1996;**39**:141-64.

[100] Sprague EA, Luo J, Palmaz JC. Endothelial cell migration onto metal stent surfaces under static and flow conditions. *J Long Term Eff Med Implants*, 2000;**10**:97-110.

[101] Srinivas K, Nakayama T, Ohta M*, et al.* Studies on Design Optimization of Coronary Stents. *Journal of Medical Devices*, 2008;**2**:011004.

[102] Stehbens WE. Etiology of intracranial berry aneurysms. *J Neurosurg*, 1989;**70**(6):823-31.

[103] Steigen TK, Maeng M, Wiseth R*, et al.* Randomized study on simple versus complex stenting of coronary artery bifurcation lesions: the Nordic bifurcation study. *Circulation*, 2006;**114**(18):1955-61.

[104] Steinberg DH, Mishra S, Javaid A*, et al.* Comparison of effectiveness of bare metal stents versus drug-eluting stents in large (> or =3.5 mm) coronary arteries. *Am J Cardiol*, 2007;**99**:599-602.

[105] Stergiopulos N, Segers P, Westerhof N. Use of pulse pressure method for estimating total arterial compliance in vivo. *Am J Physiol*, 1999;**276**:H424-8.

[106] Stone PA, Campbell JE, Aburahma AF*, et al.* Ten-year experience with renal artery in-stent stenosis. *J Vasc Surg*, 2011;**53**:1026-31.

[107] Tanaka H, Fujita N, Enoki T*, et al.* Relationship between variations in the circle of Willis and flow rates in internal carotid and basilar arteries determined by means of magnetic resonance imaging with semiautomated lumen segmentation: reference data from 125 healthy volunteers. *AJNR*, 2006;**27**:1770-5.

[108] Tang BT, Cheng CP, Draney MT*, et al.* Abdominal aortic hemodynamics in young healthy adults at rest and during lower limb exercise: quantification using image-based computer modeling. *Am J Physiol Heart Circ Physiol*, 2006;**291**(2):H668-76.

[109] Van Belle E, Tio FO, Couffinhal T*, et al.* Stent endothelialization: time course, impact of local catheter delivery, feasibility of recombinant protein administration, and response to cytokine expedition. *Circulation*, 1997;**95**(2):438-448.

[110] van Haaften AC, Bots ML, Moll FL*, et al.* Therapeutic options for carotid in-stent restenosis: review of the literature. *J Vasc Interv Radiol*, 2010;**21**:1471-7.

[111] Van Huis GA, Sipkema P, Westerhof N. Coronary input impedance during cardiac cycle as determined by impulse response method. *Am J Physiol*, 1987;**253**(2 Pt 2):H317-24.

[112] Vignon-Clementel IE, Alberto Figueroa C, Jansen KE*, et al.* Outflow boundary conditions for three-dimensional finite element modeling of blood flow and pressure in arteries. *CMAME*, 2006;**195**:3776-3796.

[113] Wang WQ, Liang DK, Yang DZ*, et al.* Analysis of the transient expansion behavior and design optimization of coronary stents by finite element method. *J Biomech*, 2006;**39**(1):21-32.

[114] Wanke I, Doerfler A, Schoch B*, et al.* Treatment of wide-necked intracranial aneurysms with a self-expanding stent system: initial clinical experience. *AJNR*, 2003;**24**(6):1192.

[115] Wentzel JJ, Whelan DM, van der Giessen WJ*, et al.* Coronary stent implantation changes 3-D vessel geometry and 3-D shear stress distribution. *J Biomech*, 2000;**33**(10):1287-95.

[116] Williams AR. Quantifying Hemodynamic Changes Caused by Stenting of Coronary Bifurcation Lesions Using Realistic Computational Fluid Dynamics Models. *Biomedical Engineering*. Master of Science: Marquette University, 2008.

[117] Williams AR, Koo BK, Gundert TJ*, et al.* Local hemodynamic changes caused by main branch stent implantation and subsequent virtual side branch balloon angioplasty in a representative coronary bifurcation. *J Appl Physiol*, 2010;**109**:532-40.

[118] Wilson N, Wang K, Dutton R*, et al.* A software framework for creating patient specific geometric models from medical imaging data for simulation based medical planning of vascular surgery. Springer, 2001:449-456.

[119] Yang W, Feinstein JA, Marsden AL. Constrained optimization of an idealized Y-shaped baffle for the Fontan surgery at rest and exercise. *CMAME*, 2010;**199**:2135-2149.

[120] Zahedmanesh H, Lally C. Determination of the influence of stent strut thickness using the finite element method: implications for vascular injury and in-stent restenosis. *Med Biol Eng Comput*, 2009;**47**:385-93.

[121] Zahn R, Hamm CW, Schneider S*, et al.* Incidence and predictors of target vessel revascularization and clinical event rates of the sirolimus-eluting coronary stent (results from the prospective multicenter German Cypher Stent Registry). *Am J Cardiol*, 2005;**95**:1302-8.

COMPUTATIONAL MODELS AND SOURCE CODE

The patient-specific stent models, code for advanced quantification methods and code implemented within the optimization framework is available by contacting Timothy Gundert at (920) 979-9673 or Dr. John F. LaDisa, PhD in the Department of Biomedical Engineering at Marquette University.